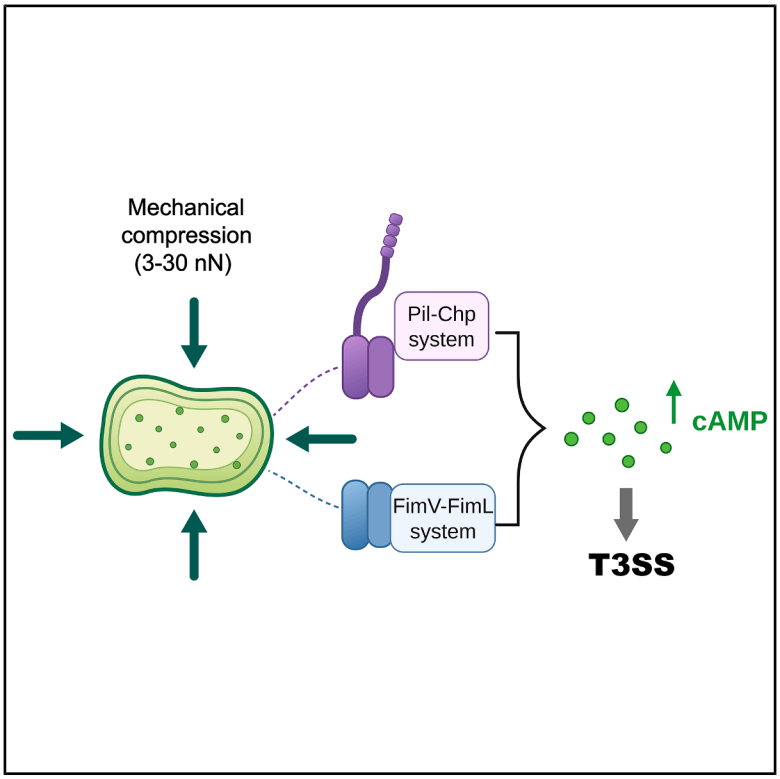
Cell Reports

Article

Mechanical compression activates cAMP signaling in *Pseudomonas aeruginosa*

Graphical abstract



Authors

Lei Ni, Yajia Huang, Yaoxin Huang, ..., Shuqiang Huang, Haiyi Liang, Fan Jin

Correspondence

yj.huang@siat.ac.cn (Y.H.), hyliang@ustc.edu.cn (H.L.), fan.jin@siat.ac.cn (F.J.)

In brief

Ni et al. show that mechanical compression activates cAMP signaling in *Pseudomonas aeruginosa* through a pathway involving CyaB, the Pil-Chp system, and the FimV-FimL module. This response links confined bacterial growth to increased T3SS-associated transcription.

Highlights

- Mechanical compression induces rapid cAMP elevation in *Pseudomonas aeruginosa*
- Compression-induced cAMP signaling requires CyaB, Pil-Chp, and FimV-FimL
- Surface piliation is dispensable, whereas PilA remains required for the response
- Compressed-state growth promotes upregulation of T3SS-associated genes

Ni et al., 2026, Cell Reports *45*, 118114
October 27, 2026 © 2026 The Author(s). Published by Elsevier Inc.
https://doi.org/10.1016/j.celrep.2026.118114

CellPress

Cell Reports

CellPress
OPEN ACCESS

Article

Mechanical compression activates cAMP signaling in *Pseudomonas aeruginosa*

Lei Ni,[1,2,6] Yajia Huang,[1,2,6,*] Yaoxin Huang,[3] Yue Yu,[1,2] Jiarui Xiong,[5] Hui Wen,[1,2] Wenwen Xiao,[1,2] Bing Li,[1,2] Shuqiang Huang,[1,2] Haiyi Liang,[3,4,*] and Fan Jin[1,2,7,*]

[1]State Key Laboratory of Quantitative Synthetic Biology, Shenzhen Institute of Synthetic Biology, Shenzhen Institutes of Advanced Technology, Chinese Academy of Sciences, Shenzhen 518055, China

[2]Shenzhen Synthetic Biology Infrastructure, Shenzhen Institute of Synthetic Biology, Shenzhen Institutes of Advanced Technology, Chinese Academy of Sciences, Shenzhen 518055, China

[3]CAS Key Laboratory of Mechanical Behavior and Design of Materials, Department of Modern Mechanics, University of Science and Technology of China, Hefei 230026, China

[4]School of Civil Engineering, Anhui Jianzhu University, Hefei 230601, China

[5]Hefei National Research Center for Physical Sciences at the Microscale, Department of Polymer Science and Engineering, University of Science and Technology of China, Hefei 230026, China

[6]These authors contributed equally

[7]Lead contact

*Correspondence: yj.huang@siat.ac.cn (Y.H.), hyliang@ustc.edu.cn (H.L.), fan.jin@siat.ac.cn (F.J.)

https://doi.org/10.1016/j.celrep.2026.118114

SUMMARY

In *Pseudomonas aeruginosa*, cyclic AMP (cAMP) is a central regulator of virulence, including the type III secretion system (T3SS), yet the signals that activate cAMP remain incompletely understood. Using the real-time cAMP biosensor Gflamp1, we show that mechanical compression elevates cAMP, with an estimated activation force of approximately 3–30 nN. This mechanoresponse requires the Pil-Chp system, the FimV-FimL module, and the adenylate cyclase CyaB. Productive surface piliation and pilus extension or retraction are dispensable, whereas the major pilin PilA remains required. We further show that the histidine kinase ChpA interacts with the polar scaffold FimV and that FimL modulates FimV-dependent ChpA polar localization. Fluorescence lifetime imaging microscopy-Förster resonance energy transfer (FLIM-FRET) analysis supports compression-dependent changes in the apparent proximity of ChpA to PilG and FimL. Finally, compressed-state growth increases T3SS-associated transcription, suggesting that compression-induced cAMP signaling may link confined growth to virulence-associated gene expression.

INTRODUCTION

The second messenger cyclic AMP (cAMP) is a central regulatory node in *Pseudomonas aeruginosa*, coordinating surface-associated motility, virulence-factor expression, and host infection programs. Early studies established an adenylate cyclase-dependent pathway in which cAMP acts through the transcription factor Vfr to regulate multiple virulence-associated traits, including type IV pili (T4Ps), the type II and type III secretion systems (T2SS and T3SS), and secreted virulence factors.[1–3] Because T3SS enables *P. aeruginosa* to inject effector proteins into host cells and is strongly associated with acute infection, defining the environmental cues that control cAMP synthesis is critical for understanding how this pathogen couples colonization state to virulence activation.

Intracellular cAMP levels in *P. aeruginosa* are controlled by two adenylate cyclases, CyaA and CyaB, and by the cAMP phosphodiesterase CpdA, which degrades cAMP to maintain homeostasis.[3–5] CyaB is particularly important for surface-associated cAMP responses and is regulated by the Pil-Chp chemosensory system.[5–7] A major framework for cAMP regulation has emerged from studies of T4P-dependent surface sensing. T4Ps dynamically extend, attach, and retract, powering twitching motility while allowing cells to probe physical interfaces.[6,8] The Pil-Chp pathway links T4P activity to cAMP production through the MCP-like receptor PilJ, the histidine kinase ChpA, and the response regulators PilG and PilH.[5,6,9,10] A mechanochemical model proposed that interactions between the major pilin PilA and PilJ allow T4P attachment and retraction to regulate cAMP/Vfr signaling.[6] Subsequent work showed that surface stiffness can tune cAMP/Vfr output through T4P-mediated surface deformation, extending surface sensing from contact detection to mechanical discrimination.[11] More recent studies further implicated the retraction motor PilT in transmitting surface signals to PilJ and showed that PilJ is dynamically regulated by PilK- and ChpB-dependent methylation, which modulates

This is an open access article under the CC BY-NC-ND license (http://creativecommons.org/licenses/by-nc-nd/4.0/).

both cAMP output and twitching reversals during Pil-Chp surface sensing.[12,13] Beyond cAMP regulation, the Pil-Chp system also directs surface motility: surface-attached *P. aeruginosa* cells bias twitching movement along chemical gradients, and recent studies identified PilJ as a T4P-linked chemoreceptor that guides responses to interspecies peptide signals and enables spatial sensing during pili-based chemotaxis.[14–16] Thus, the Pil-Chp system acts as an interface-localized module that integrates mechanical, chemical, and motility-related cues.

In parallel with Pil-Chp, the FimV-FimL-PilG axis provides an additional layer of polar organization and cAMP regulation. FimV is a polar scaffolding protein containing a peptidoglycan-binding LysM motif and C-terminal tetratricopeptide repeat domains, which support both cAMP-dependent and cAMP-independent functions.[17–19] FimL binds both FimV and PilG, linking the polar scaffold to the response regulator that stimulates CyaB-dependent cAMP synthesis.[17] Because FimV is connected to the cell envelope and peptidoglycan, the FimV-FimL-PilG complex provides a plausible route through which changes in cell-envelope geometry could influence PilG activity and cAMP production.

Surface sensing also intersects with c-di-GMP-dependent attachment and PilY1-mediated mechanosensing. In one model, cAMP acts early after surface contact through Vfr and FimS-AlgR to promote T4P deployment and early surface behaviors, whereas c-di-GMP rises later to drive irreversible attachment and biofilm-associated phenotypes.[7] The T4P machinery-associated diguanylate cyclase SadC, through interactions involving PilO, links T4P assembly to c-di-GMP production during early biofilm formation.[20] In parallel, the T4P-associated adhesin PilY1 can undergo force-induced conformational changes in its vWA domain, supporting its role as a mechanosensitive element in surface sensing.[21,22] Together, these studies indicate that *P. aeruginosa* uses multiple T4P-associated systems to convert surface contact, force, and motility state into coordinated second-messenger outputs.

Despite these advances, most studies of cAMP dynamics in *P. aeruginosa* have relied on transcriptional reporters, whose kinetics are constrained by transcription, translation, and bacterial growth. These reporters are well suited for measuring integrated downstream pathway activation but cannot resolve rapid or transient cAMP fluctuations that may occur during surface exploration, collective motility, or mechanical perturbation. To overcome this limitation, we used Gflamp1, a circularly permuted fluorescent protein (cpFP) that reversibly binds cAMP and rapidly changes fluorescence, enabling real-time monitoring of intracellular cAMP dynamics.[23]

Applying this approach to a gel-glass interface assay, we unexpectedly observed a population-wide elevation of cAMP when bacterial populations became densely packed and traffic jammed, rather than during initial surface contact. We further found that this response does not require surface-exposed T4P filaments but is triggered by mechanical compression forces that accumulate during bacterial growth. Using gel microcavities, microfluidic compression, genetic perturbations, and fluorescence lifetime imaging microscopy-Förster resonance energy transfer (FLIM-FRET) analysis, we show that compression-induced cAMP signaling requires CyaB, the Pil-Chp system, and the FimV-FimL module. We further provide evidence that ChpA associates with FimV and PilG, that FimL modulates ChpA polar localization, and that compression alters the apparent proximity among components of this polar signaling module. Finally, we show that compressed-state growth is followed by the upregulation of T3SS-associated transcription. These findings reveal mechanical compression as a previously underappreciated input into cAMP signaling and suggest a mechanism by which densely colonized bacteria activate virulence-associated programs within confined host environments.

RESULTS

Coordinated cAMP elevation upon bacterial traffic jamming at gel-glass interface

To investigate the rapid temporal dynamics of cAMP fluctuations within *P. aeruginosa* cells, we employed Gflamp1, a highly sensitive and specific monomeric cpFP sensor.[23] With a dissociation constant of ~2 μM, Gflamp1 aligns with the physiological range of cAMP concentration in *P. aeruginosa*. We fused Gflamp1 to CyOFP1 (Figure S1A), a fluorescent protein with constant fluorescence independent of cAMP concentration,[24] enabling normalization of the Gflamp1 signal for variations in cell density and bacterial colony thickness. *In vitro* calibration of the purified fusion protein confirmed that its fluorescence ratio was sensitive to cAMP concentration, with a Hill coefficient of 0.9 and an apparent half-maximal effective concentration (EC50) of approximately 1.4 μM (Figure S2). Previous studies have shown that deletion of *cpdA*, which encodes a cAMP phosphodiesterase in *P. aeruginosa*, or deletion of *pilH*, which encodes a CheY-like response regulator in the Pil-Chp system, increases intracellular cAMP levels, whereas removal of the adenylate cyclase genes *cyaA* and *cyaB* decreases intracellular cAMP levels.[4,5] Using cells harvested from liquid shaking cultures at the exponential growth phase, we observed Gflamp1/CyOFP1 ratios of about 0.74, 1.28, 1.78, and 0.43 in wild-type, Δ*cpdA*, Δ*pilH*, and Δ*cyaA*Δ*cyaB* cells, respectively (Figure S1B). These values are consistent with previous measurements of altered cAMP levels in these mutants,[4,5] indicating that the Gflamp1/CyOFP1 ratio serves as a semiquantitative readout of intracellular cAMP levels in *P. aeruginosa*.

We started with a widely used experimental setup in which wild type *P. aeruginosa* cells were allowed to grow between agarose gel and coverglass using the fastidious anaerobe broth (FAB) medium (see STAR Methods for details). Initially, bacterial cells exhibited colony expansion across the interface, with substantial cell-to-cell heterogeneity in the Gflamp1/CyOFP1 signal, wherein fluctuations could be observed within certain individual cells (Video S1). We observed the previously reported early increase in cAMP levels[6,7] during the early surface-attached stage (0–6 h). At a later stage, the bacteria transitioned into rapid, fluid-like motility across the entire interface, accompanied by an overall attenuation of the Gflamp1/CyOFP1 signal (Figures 1A and 1B, points ii and iii). Remarkably, as the cells gradually became densely packed and traffic-jammed, we observed a coordinated population-wide elevation in Gflamp1/CyOFP1 (Figures 1A and 1B, points v and vi).

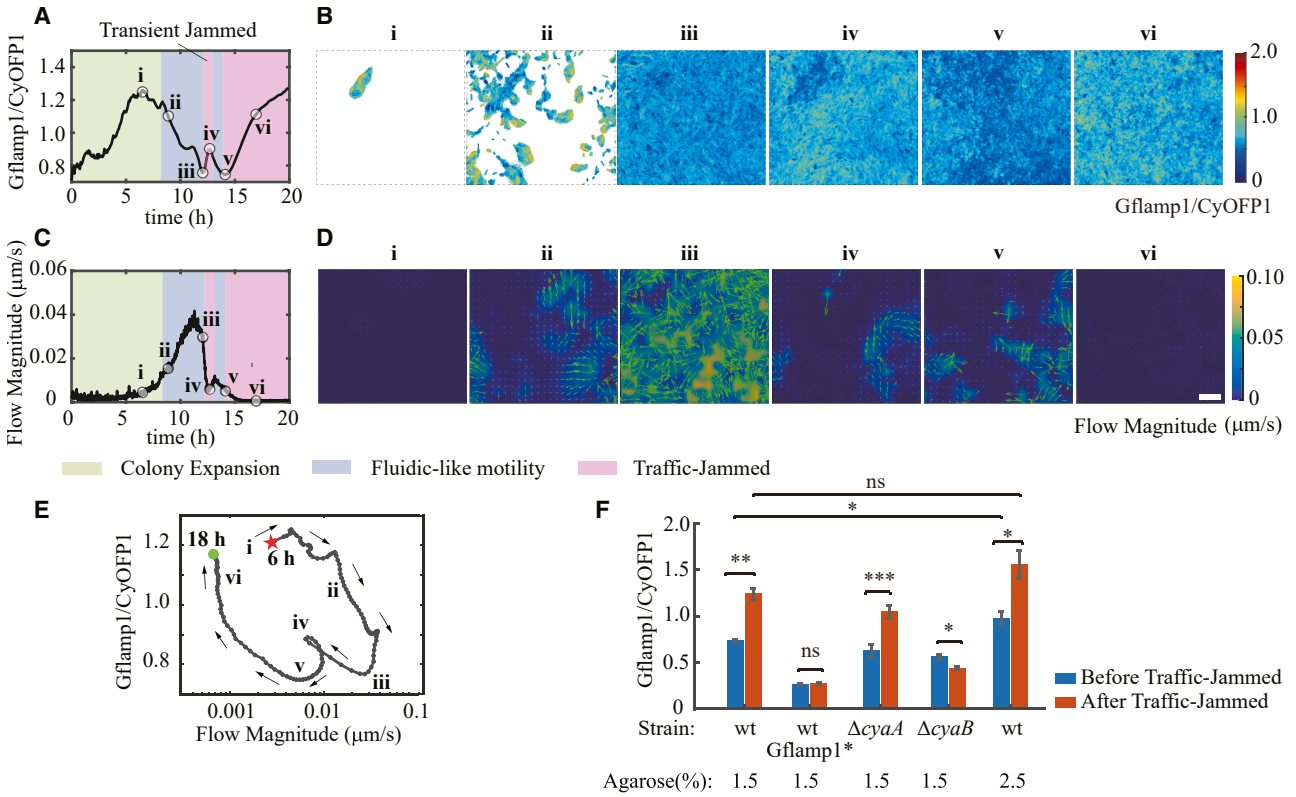


Figure 1. Coordinated cAMP elevation upon bacterial traffic jamming at the gel-glass interface

(A) Time series of cell-average Gflamp1/CyOFP1 for wild-type *P. aeruginosa* grown at the hydrogel-glass interface. Shaded green region indicates colony expansion phase; pale blue region, fluid-like motility phase; pink region, traffic-jammed phase.

(B) Spatial patterns of Gflamp1/CyOFP1 at six time points (i–vi) corresponding to the bold roman letters marked in (A).

(C) Temporal variation of particle-averaged flow magnitude corresponding to data in (A), calculated using the PIVlab tool from bacterial CyOFP1 fluorescence images.

(D) Spatial patterns of flow magnitude at six time points (i–vi) corresponding to the bold roman letters marked in (A) and (C). For data visualization, velocity magnitude heat maps were superimposed with the corresponding vector fields. Scale bars, 20 μm.

(E) Gflamp1/CyOFP1 plotted as a function of flow magnitude using data collected from 6 to 18 h in (A).

(F) Gflamp1/CyOFP1 for various strains before and after entering the totally jammed state. $n = 2$ fields of view for wild type (WT) 1.5%, WT 2.5%, and Δ*cyaB*, and $n = 6$ fields of view for Δ*cyaA* and WT expressing Gflamp1*. All fields of view were obtained from a single experimental run. Statistical significance between the pre-jammed and totally jammed states was determined using a two-sample *t* test; ***$p < 0.001$, **$p < 0.01$, *$p < 0.05$; ns, non-significant. Data are presented as mean ± SD.

To characterize the motility dynamics of bacteria at the interface, we modeled collectively moving bacteria as tracers in a flow field and applied particle image velocimetry (PIV) to extract flow velocities from time-series CyOFP1 fluorescence images. As expected, bacteria underwent high-velocity motion during the interval from point ii to iii (Figures 1C and 1D). Subsequently, from point iii to iv, bacterial flow magnitude dropped dramatically, corresponding to a brief rise in the Gflamp1/CyOFP1 signal—a period we designated as the transient jammed phase. In general, bacterial flow magnitude and the Gflamp1/CyOFP1 signal exhibited approximately opposite trends (Figure 1E). Together, these results indicate that our assay captures a delayed, growth-induced jamming-associated cAMP response at high cell density, distinguishing it from the early surface-sensing response described previously.

Previous work has shown that *P. aeruginosa* can sense surface stiffness through T4Ps and consequently regulate intracellular cAMP levels.[11] We therefore examined the cAMP response of bacteria under higher agarose concentration. We found that, although the basal cAMP level was higher, the traffic-jamming-induced cAMP increase was similar to that observed under the softer condition (Figure 1F). Deletion of *cyaB*, but not *cyaA*, or the use of a cAMP-non-binding Gflamp1* (Gflamp1:R307W) variant,[25] abolished the increase in fluorescence ratio upon bacterial traffic jamming (Figure 1F), indicating that bacteria upregulate cAMP synthesis via CyaB.

cAMP elevation does not depend on species-specific signaling or surface-exposed T4Ps

We next studied the potential cues that trigger the cAMP response in *P. aeruginosa*. Repeating the observation using the quorum sensing-deficient Δ*lasI*Δ*rhlI* strain between the gel-glass interface revealed a similar cAMP elevation after the cells became traffic jammed (Figure 2A). We co-cultured *P. aeruginosa* with

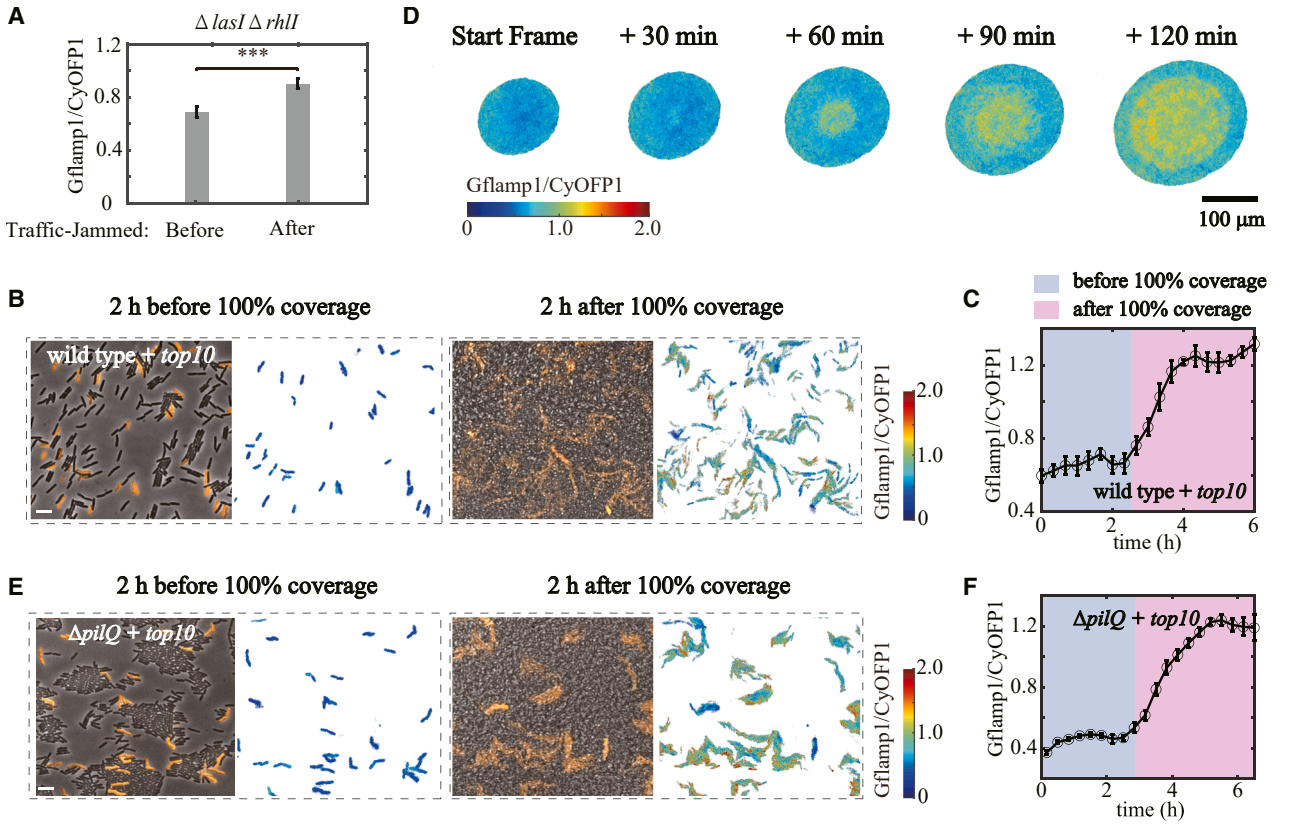


Figure 2. cAMP elevation does not depend on species-specific signaling or surface-exposed type IV pili

(A) Changes in the Gflamp1/CyOFP1 ratio in the quorum-sensing-deficient Δ*lasI*Δ*rhlI* strain before and after cells entered the traffic-jammed state at the gel-glass interface. $n = 4$ fields of view were obtained from a single experimental run. Statistical significance was determined using a two-tailed t test; $^{***}p < 0.001$. Data are presented as mean ± SD.

(B) Phase-contrast and Gflamp1/CyOFP1 ratio images of mixed cultures of *E. coli* and wild-type *P. aeruginosa* cells at the gel-glass interface. *P. aeruginosa* cells were identified by CyOFP1 fluorescence, shown in orange in the phase-contrast images. Images were acquired 2 h before and after the bacteria filled the field of view. Scale bars, 5 μm.

(C) Temporal variation in the cell-averaged Gflamp1/CyOFP1 ratio corresponding to the experiment shown in (B). Data are presented as mean ± SD.

(D) Spatial dynamics of the Gflamp1/CyOFP1 ratio in Δ*pilQ* cells during growth at the gel-glass interface.

(E) Phase-contrast and Gflamp1/CyOFP1 ratio images of mixed cultures of *E. coli* and *P. aeruginosa* Δ*pilQ* cells at the gel-glass interface.

(F) Temporal variation in the cell-averaged Gflamp1/CyOFP1 ratio corresponding to the experiment shown in (E). Data are presented as mean ± SD. Scale bars in (B) and (E), 5 μm; scale bar in (D), 100 μm.

Escherichia coli cells at a 1:10 ratio beneath agarose pads and again observed the increase in Gflamp1/CyOFP1 signal within *P. aeruginosa* cells after cells became densely packed (Figures 2B and 2C; Video S2). These results suggest that the accumulation of species-specific signaling molecules like autoinducers is unlikely to contribute to the observed coordinated elevation of bacterial intracellular cAMP. We further tested whether flagella contribute to this response by examining the Δ*fliC* mutant. Loss of *fliC* altered the colony expansion pattern and weakened fluid-like movement at the gel-glass interface, indicating that flagella contribute to interfacial motility (Figure S3A). However, Δ*fliC* cells still showed a significant increase in Gflamp1/CyOFP1 after entering the traffic-jammed state (Figure S3B), suggesting that flagella-dependent motility is not required for the traffic-jamming-associated cAMP response.

Previous studies have demonstrated that *P. aeruginosa* can sense surfaces through its T4Ps and consequently upregulate intracellular cAMP levels.[6,7,26] We repeated the aforementioned *E.coli-P. aeruginosa* co-culture assay using the Δ*pilQ* strain, which lacks the outer membrane secretin required for T4P assembly, with no detectable surface-exposed pili under our imaging conditions (Video S3). In gel-glass interface cultures of the single strain, the fluid-like motion stage was absent, with colony expansion becoming the dominant mode throughout the observation period. Interestingly, at the later stage of colony growth, cells also exhibited a large-scale, coordinated increase in Gflamp1/CyOFP1 that emerged from the colony center and propagated toward the periphery (Figure 2D; Video S4). In co-culture experiments with *E. coli*, we similarly observed an increase in Gflamp1/CyOFP1 after bacteria filled the field of view (Figures 2E and 2F; Video S2). These results indicate that productive pilus extension and retraction are not strictly required for the observed response. We consider that there may be some underlying mechanisms

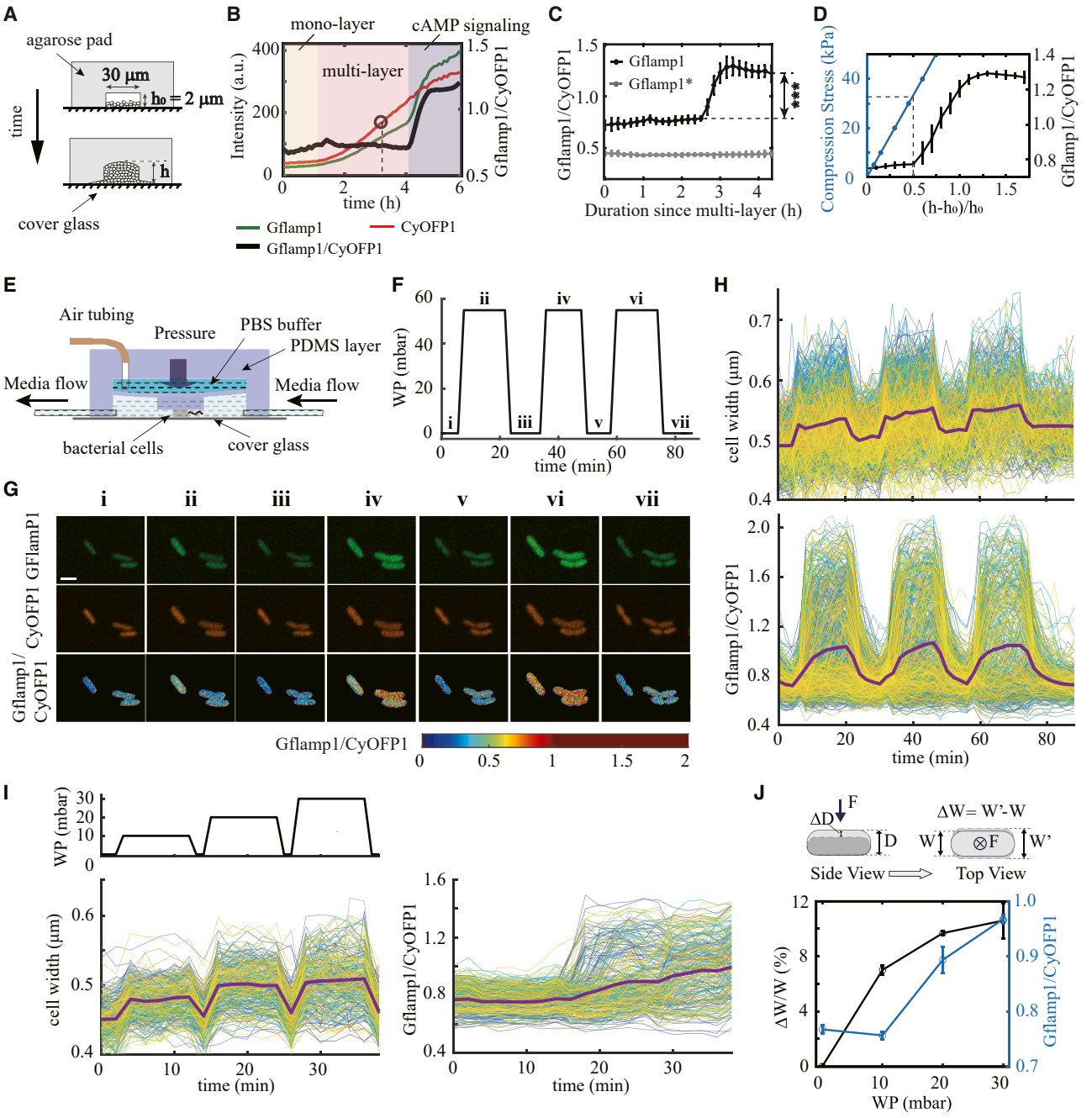


Figure 3. Mechanical compression activates bacterial cAMP signaling

(A) Schematic diagram of bacterial cells grown in agarose microcavities.

(B) Temporal dynamics of Gflamp1, CyOFP1, and Gflamp1/CyOFP1 signals as Δ*pilQ* cells grew within gel microcavities. The black circle in the multilayer phase marks when CyOFP1 intensity reaches four times that of the single-layer phase, corresponding to when the bacteria have just filled the microcavity.

(C) Time-resolved Gflamp1/CyOFP1 curves of Δ*pilQ* strains expressing Gflamp1 or Gflamp1(R307W) during growth in microcavities. Data are presented as mean ± SD. ***p < 0.001, *p < 0.01, p < 0.05; ns, not significant. Statistical comparisons between two groups were performed using a two-sample t test.

(D) Relationship between gel apparent strain, compressive stress, and mean Gflamp1/CyOFP1 signal in the microcavity experiment. Data are presented as mean ± SD.

(E) Schematic diagram of the microfluidic device designed for direct bacterial compression.

(F–H) Experimental results from compressing Δ*pilQ* cells using the cyclic working-pressure curve shown in (F). WP, working pressure.

(legend continued on next page)

that trigger a cAMP response following bacterial growth to a crowded, compressed state.

Mechanical compression activates bacterial cAMP signaling

It has been previously established that when cells proliferate within confined spaces to reach a jammed state, there is a swift buildup of mechanical forces, and the collapse of these force chains results in a rapid reduction of the mechanical forces.[27] In Figure 1, Gflamp1/CyOFP1 signal rose and fell as bacterial cells briefly jammed before resuming a fluidic state, aligning with the mechanical force changes noted in the aforementioned research. We proceeded to investigate whether mechanical compression could induce cAMP signaling in *P. aeruginosa*. Given that twitching motility mediates collective migration of cells, which will lead to constantly changing compaction states within the population,[8,28] and T4P dynamics could potentially modulate cAMP signaling,[6,11] we chose the non-piliated *pilQ* mutant for subsequent experiments.

Two experimental setups were designed to explore the effects of mechanical compression. In the first, the gel-glass experimental system was slightly modified by introducing microcavities (2 μm height, 30 μm in diameter) on the gel surface (Figure 3A), so that cells grown within it could enter a compressed state with a sharper transition upon pushing against the chamber wall. As shown in Figure 3B, cells in microcavities grew from monolayer to multilayer, with increasing CyOFP1 signal due to vertical stacking, while Gflamp1/CyOFP1 remained constant initially. About 1 h after the cavities were filled (four cell layers), Gflamp1/CyOFP1 increased rapidly and plateaued (Video S5). This is much earlier than cAMP signaling observed in Figure 2D. Replacing Gflamp1 with the cAMP-insensitive variant Gflamp1* abolished the fluorescence-ratio change (Figure 3C; Video S5). To independently validate the microcavity results, we also employed a widely used *lac* transcriptional reporter and observed a similar response (Figure S4), further confirming that the signal specifically reflects cAMP. An increase in the Gflamp1/CyOFP1 ratio was also observed when the gel microcavity assay was performed in lysogeny broth (LB) medium (Figure S5), suggesting that the compression-associated cAMP response is not specific to FAB medium. We identified a transition point for the cAMP response at an apparent gel strain of $\frac{h-h_0}{h_0} \approx 0.5$ (Figure 3D). Based on a simplified physical model, the compressive stress exerted on cells was estimated to be ~30 kPa using the agarose modulus measured by Normand et al.[29]; when a lower reported agarose modulus was used,[11] this estimate decreased to ~12 kPa (see supplemental information). Assuming an effective load-bearing area of approximately $1\mu m^2$ per cell, these stress estimates correspond to a characteristic compressive force scale of approximately 12–30 nN. Notably, cells within microcavities consistently showed an earlier cAMP increase than nearby cells outside the cavities (Figure S6), which also suggests that bacteria are responding to mechanical compression.

In the second experimental setup, we used a microfluidic device to directly apply mechanical pressure to bacterial cells (Figures 3E and S7). The device consists of two chambers separated by an 80-μm-thick polydimethylsiloxane (PDMS) membrane bearing square compression pillars on its underside. The upper chamber is filled with PBS and connected to an air-pressure controller, whereas the lower chamber forms a flow cell for bacterial cultivation. When pressure is applied, the membrane deforms downward, and the pillars directly compress the cells beneath them. We designed a cyclic working pressure profile alternating between 55 mbar for 16 min and 0 mbar for 10 min (Figure 3F). Cells widened under high working pressure (Figures 3G and 3H), confirming successful pressure-induced deformation. We observed that both the average Gflamp1/CyOFP1 ratio and cell width closely tracked the working-pressure profile (Figures 3F–3H; Video S6; Figures S8A–S8C). Repeating the experiments using Gflamp1* abolished the Gflamp1/CyOFP1 response while preserving the compression-induced width changes (Figure S9). As an independent validation, we monitored *lac* promoter activity during sustained direct compression and observed a marked increase beginning approximately 1 h after compression onset, with little change under non-compression conditions (Figure S10). These results demonstrate that using mechanical compression as the sole stimulus is sufficient to elevate bacterial intracellular cAMP levels. To determine the threshold of mechanical force to trigger the cAMP response, we incrementally increased the working pressure in steps. The Gflamp1/CyOFP1 signal began to increase when cell deformation reached approximately 7%–9% (Figures 3I and 3J). Based on the pressurized-shell indentation model,[30] this deformation corresponds to an estimated mechanical force of 3–30 nN, depending on the assumed bacterial turgor pressure (see STAR Methods for calculation details). This force range is broadly consistent with the characteristic 12–30 nN scale estimated for the microcavity assay.

In the microfluidic device, although pressure was applied vertically, cells underwent lateral displacement during compression and frequently formed multicellular clusters (Figure S11). When grouped according to cluster size, cells in larger clusters exhibited cAMP responses more frequently than isolated cells or cells in smaller groups (Figure S11). Under a slowly varying sinusoidal pressure waveform, the cAMP response was first detected near the cluster center as pressure increased and subsequently extended toward the periphery; during unloading, the responding region progressively retracted (Figure S12A).

(G) Representative time-lapse images showing Gflamp1, CyOFP1, and Gflamp1/CyOFP1 signals. Scale bars, 2 μm. Roman numerals correspond to time points in (F).

(H) Compiled single-cell data (thin lines) and average values (thick magenta line) for changes in bacterial width and Gflamp1/CyOFP1 signal. Different colors of thin lines represent data from different individual cells.

(I) Response of bacterial width and Gflamp1/CyOFP1 signal under stepwise increasing working pressure.

(J) Schematic illustration of bacterial deformation and the mechanical force (marked near the $\Delta W/W$ curve) exerted on cells under compression, based on data in (I). Data are presented as mean ± SD.

Most cells within the cluster responded during the compression cycle, although the timing and magnitude of the response varied with spatial position. Notably, the cAMP signal in cells near the cluster center increased and subsequently decreased during the pressure cycle (Figure S12B). Together, these observations suggest that in-plane cell-cell forces generated within bacterial clusters may contribute to cAMP activation. Differences in the local mechanical loads experienced by individual cells can also partly account for the cell-to-cell heterogeneity in the cAMP response during compression.

To further determine whether productive T4P activity is required for the compression-associated cAMP response, we examined mutants defective in major components of the T4P system. In gel microcavities, deletion of *pilA* largely abolished the increase in the Gflamp1/CyOFP1 ratio during multilayer growth, whereas Δ*pilB*, Δ*pilT*, and Δ*pilY1* cells retained cAMP responses, although the response magnitude varied among these mutants (Figure S13A). A similar pattern was observed during direct microfluidic compression: Δ*pilA* cells failed to show a compression-induced cAMP increase, whereas mutants lacking the PilB extension motor, the PilT retraction motor, or PilY1 retained the response to varying degrees (Figure S13B). These results indicate that T4P extension and retraction are not required for compression-induced cAMP activation, whereas the major pilin PilA remains necessary.

We also examined wild-type cells under gel microcavity and direct-compression conditions. Wild-type cells showed a transient cAMP increase in gel microcavities but subsequently moved out of the cavity as small clusters and showed a weaker average response than Δ*pilQ* cells under direct microfluidic compression (Figures S13B and S14). A compression-induced cAMP response was still observed in the flagella-deficient Δ*pilQ* Δ*fliC* double mutant, although the response was slightly reduced compared with Δ*pilQ* cells (Figure S15). Together, these results indicate that growth-induced mechanical compression is sufficient to trigger the population-wide cAMP response shown in Figure 1B.

Both the Pil-Chp system and the FimV-FimL module are required for bacterial response to mechanical compression

Next, we investigated the intracellular signaling pathways underlying the observed cAMP response. *P. aeruginosa* has two adenylate cyclases, CyaA and CyaB,[3] responsible for cAMP synthesis, and a single phosphodiesterase, CpdA, that catalyzes cAMP degradation.[4] Through gene knockout experiments, we determined that the compression-induced fold increase in cAMP was abolished in the *cyaB* mutant strain but not in the *cyaA* or *cpdA* mutants (Figures 4A and 4B and S16; Video S5). By contrast, deletion of *cyaA* reduced the overall Gflamp1/CyOFP1 reporter level but did not substantially impair the relative fold increase induced by compression, suggesting that CyaA contributes to basal cAMP production but is not the major adenylate cyclase responsible for the compression-induced cAMP response. We also monitored the ATP sensor iATPSnFR in the gel microcavity assay and observed only a slight decrease in the iATPSnFR/CyOFP1 ratio, suggesting that the cAMP response is not attributable to elevated intracellular ATP levels (Figure S17).

In *P. aeruginosa*, phosphorylated PilG is known to promote CyaB-dependent cAMP synthesis.[5] PilG participates in at least two interacting polar protein modules (Figure 4C). In the Pil-Chp system, the methyl-accepting chemotaxis protein PilJ transduces chemical or mechanical signals to the histidine kinase ChpA, which regulates PilG phosphorylation through direct association with PilG.[5,9] In parallel, PilG binds FimL, which in turn associates with the polar scaffold FimV.[17,18] FimV is anchored to the peptidoglycan through its LysM domain,[31] providing a plausible route through which mechanically induced changes in the cell envelope could influence PilG-associated signaling. PilG polar localization is regulated by both ChpA and the FimL-FimV module.[17] However, whether PilG binds ChpA and FimL simultaneously, sequentially, or in mutually exclusive complexes remains unknown. We therefore tested *pilG*, *pilJ*, *chpA*, *fimL*, *fimV*, and *lysM* mutants for their response to mechanical compression in the microfluidic device. All of these strains were also deficient in their ability to increase cAMP levels in response to mechanical cell wall compression (Figure 4D).

The Pil-Chp system has been implicated in twitching chemotaxis, in which cells bias surface motility by modulating reversal frequency.[14,15] Recent work further suggests that PilJ methylation and demethylation are associated with twitching reversals during Pil-Chp-dependent chemotaxis.[13] In canonical chemotaxis systems, sustained stimulation is often followed by adaptation of the output toward baseline.[32] We therefore asked whether the compression-induced cAMP response exhibits similar adaptive behavior. Under sustained mechanical compression, the Gflamp1/CyOFP1 ratio remained elevated for at least 60 min, close to one cell generation time (Figure 4E), indicating that compression-induced cAMP signaling does not rapidly adapt back to baseline. Thus, the sustained cAMP response observed here likely represents a signaling mode distinct from the adaptive behavior described during conventional chemotaxis.

We further examined basal cAMP reporter levels under liquid-growth conditions in *pilG*, *pilJ*, *chpA*, *fimL*, *fimV*, and *lysM* mutants, all constructed in the Δ*pilQ* background. All of these strains showed similarly low Gflamp1/CyOFP1 ratios, close to that of the *cyaB* mutant strain (Figure 4F), indicating that both the Pil-Chp system and the FimV-FimL module are required for maintaining basal cAMP signaling. Together with the loss of the compression-associated cAMP increase in these mutants (Figure 4D), these results indicate that both modules are required for the observed response but do not distinguish a compression-specific role from a more general requirement for cAMP signaling. Because FimV binds peptidoglycan and is physically linked to the cell envelope, we next investigated FimV-associated signaling interactions as a possible route coupling envelope deformation to cAMP signaling.

ChpA associates with FimV and PilG, and its polar localization is modulated by FimL

The N-terminal region of ChpA (amino acids [aa] 8–557; $ChpA^N$) has previously been reported to share homology with FimL (Figure 5A).[33] This similarity raises the possibility that $ChpA^N$ engages some of the same binding partners as FimL, including FimV and PilG. AlphaFold3-based protein-protein interaction predictions further supported this possibility. The predicted

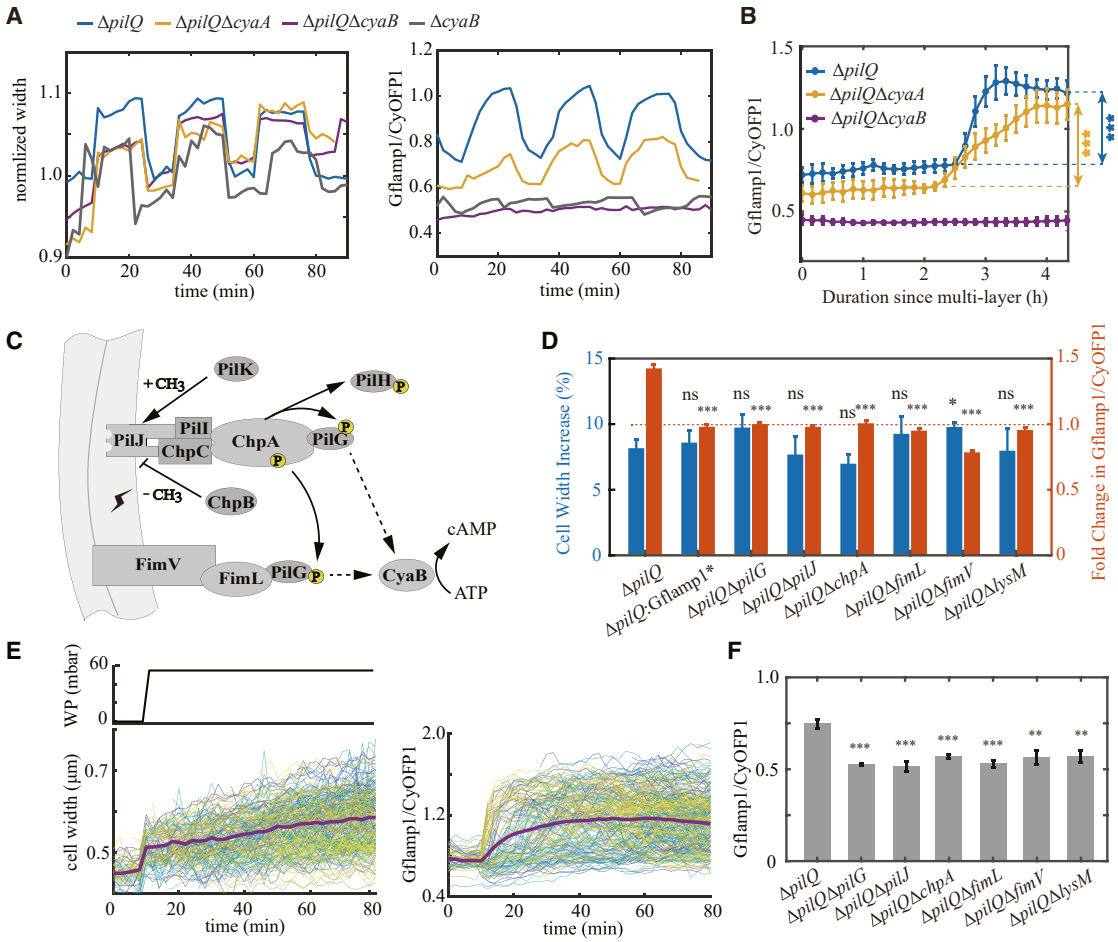


Figure 4. Both the Pil-Chp system and the FimV-FimL complex are required for the bacterial response to mechanical compression

(A) Temporal variation of average cell width and the average Gflamp1/CyOFP1 ratio in response to applied working pressure in Δ*pilQ*, Δ*pilQ*Δ*cyaA*, Δ*pilQ*Δ*cyaB*, and Δ*cyaB* strains.

(B) Quantification of the Gflamp1/CyOFP1 ratio for Δ*pilQ*, Δ*pilQ*Δ*cyaA*, and Δ*pilQ*Δ*cyaB* cells grown in agarose gel microcavities after the start point of the monolayer growth phase. Data are presented as mean ± SD. ***p < 0.001, *p < 0.01, p < 0.05; ns, not significant. Statistical comparisons between two groups were performed using a two-sample t test.

(C) Schematic of the Pil-Chp chemosensory system and the FimV-FimL-PilG module regulating CyaB activity and cAMP synthesis. The cartoon indicates that PilG is functionally connected to both ChpA and FimL, and that phosphorylated PilG promotes CyaB-dependent cAMP production.

(D) Percent increase in average cell width and fold change in the Gflamp1/CyOFP1 ratio in response to applied working pressure for Δ*pilQ*, Δ*pilQ*:Gflamp1*, Δ*pilQ*Δ*pilG*, Δ*pilQ*Δ*pilJ*, Δ*pilQ*Δ*chpA*, Δ*pilQ*Δ*fimL*, Δ*pilQ*Δ*fimV*, and Δ*pilQ*Δ*lysM* cells. Each group represents values obtained from three repeated compression cycles. Data are presented as mean ± SD.

(E) Temporal variation of cell width (left) and the Gflamp1/CyOFP1 ratio (right) of Δ*pilQ* cells in response to sustained high working pressure. Average cell width and Gflamp1/CyOFP1 values are plotted as thick magenta lines.

(F) Average Gflamp1/CyOFP1 ratio of Δ*pilQ*, Δ*pilQ*Δ*pilG*, Δ*pilQ*Δ*pilJ*, Δ*pilQ*Δ*chpA*, Δ*pilQ*Δ*fimL*, Δ*pilQ*Δ*fimV*, and Δ*pilQ*Δ*lysM* strains. Cells were grown in liquid FAB culture at 37°C with two cycles of 50× dilution-shaking and harvested at optical density 600 (OD_{600}) 0.1–0.2. Three independent experimental replicates were conducted for each strain. Statistical significance in (D) and (F) was assessed by comparing each mutant with the Δ*pilQ* strain using a two-tailed *t* test. ***$p < 0.001$, **$p < 0.01$, *$p < 0.05$; ns, non-significant. Data are presented as mean ± SD.

$ChpA^N$-PilG complex yielded an interface predicted template modeling (ipTM) score of 0.66 and a predicted template modeling (pTM) score of 0.43, whereas the predicted $ChpA^N$-TPR3 (aa 844–919) complex yielded an ipTM score of 0.76 and a pTM score of 0.45 (Table S1). The relatively high ipTM scores supported plausible interaction interfaces, although the lower pTM scores indicated uncertainty in the overall complex models. For comparison, the predicted FimL-PilG and FimL-TPR3 complexes yielded ipTM/pTM scores of 0.77/0.71 and 0.71/0.62 (Table S1), respectively. Notably, a functional connection between ChpA and PilG has also been suggested by previous observations that PilG polar localization depends on ChpA,[10] as well as by *in vitro* evidence of ChpA-dependent PilG phosphorylation.[9]

To test these potential interactions, we performed bacterial adenylate cyclase two-hybrid (BACTH) assays. $ChpA^N$ showed

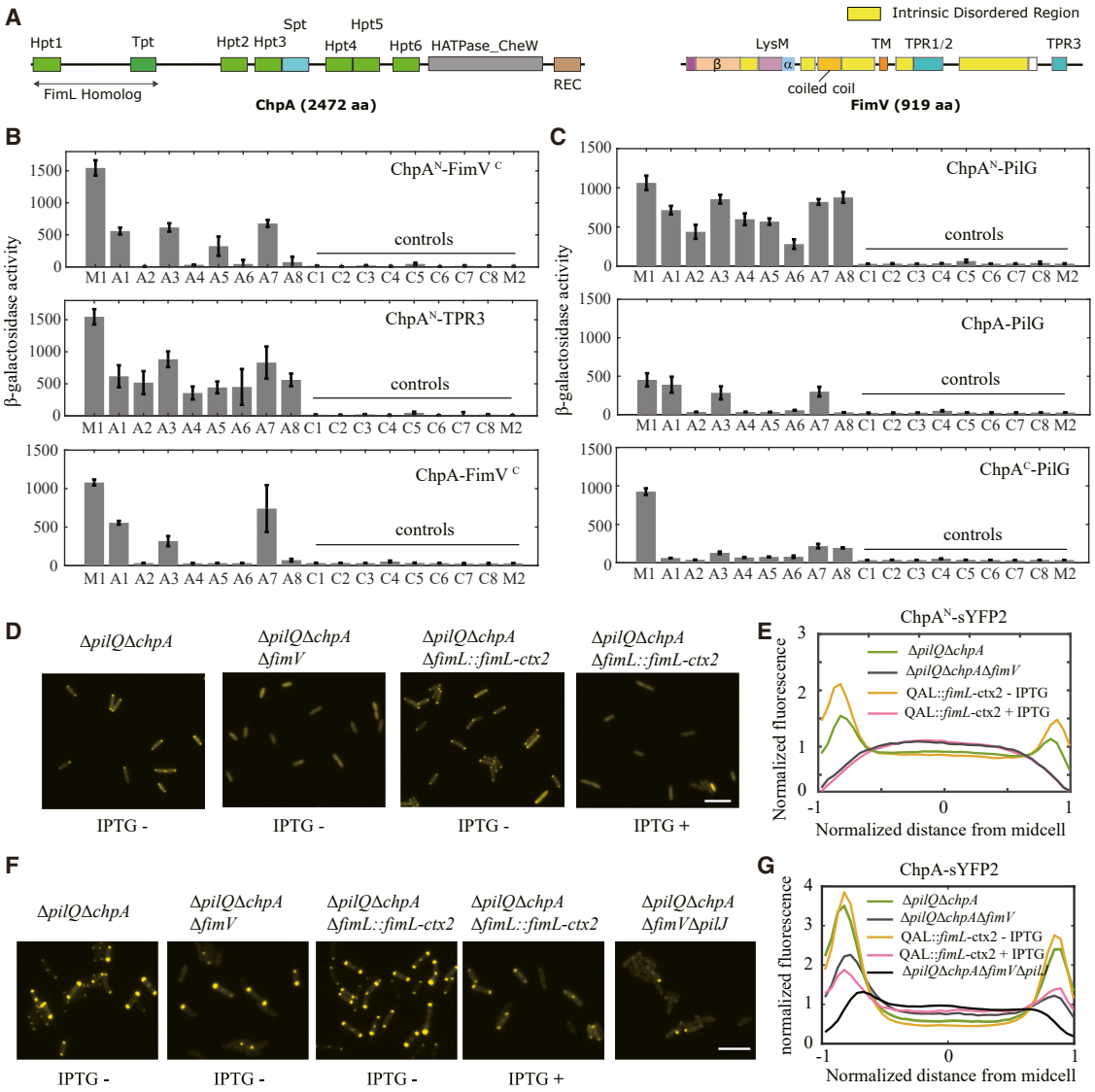


Figure 5. Interaction and localization analysis of ChpA, FimV, PilG, and FimL

(A) Domain organization of ChpA[9] and FimV proteins. FimL homolog, aa 8–557 in the N terminus of ChpA. Hpt, histidine phosphotransfer domain; Tpt, threonine phosphotransfer domain; Spt, serine phosphotransfer domain; HATPase_CheW, combined dimerization/HATPase_CheW domains; REC, response regulator receiver domain. α and β indicate α helix and β sheet domains, respectively; LysM, lysin motif domain; TM, transmembrane domain; TPR, tetratricopeptide repeat domain. Yellow regions indicate predicted intrinsically disordered regions in FimV.

(B) Bacterial adenylate cyclase two-hybrid (BACTH) assays measuring interactions between ChpA^{N} (aa 8–557) and FimV^{C} (aa 481–919), ChpA^{N} and the TPR3 domain of FimV, and full-length ChpA and FimV^{C}. M1: T18-zip + T25-zip; M2: T18 + T25. For each tested protein pair, A1–A8 indicate different N- or C-terminal fusion configurations with the T18 and T25 fragments. C1–C8 indicate the corresponding empty-vector control combinations. Data are presented as mean ± SD.

(C) BACTH assays measuring interactions between ChpA^{N} and PilG, full-length ChpA and PilG, and ChpA^{C} (aa 558–2472) and PilG. Construct designations are the same as in (B), with FimV ^{C} or TPR3 replaced by PilG as indicated. Each condition in (B) and (C) was conducted with three independent experimental replicates. Data are presented as mean ± SD.

(D and E) Representative fluorescence images and normalized cell-axis intensity profiles of ChpA^{N}-sYFP2 in the indicated genetic backgrounds and induction conditions.

(F and G) Representative fluorescence images and normalized cell-axis intensity profiles of full-length ChpA-sYFP2 in the indicated genetic backgrounds and induction conditions.

For (D)–(G), *fimL* expressed at the genomic *ctx* site was driven by an isopropyl β-D-1-thiogalactopyranoside (IPTG)-inducible promoter, and IPTG was added at a final concentration of 0.1 mM in IPTG+ groups. The *x* axis in (E) and (G) represents the normalized distance from midcell, with cell poles at −1 and 1. Exact sample sizes (cells) were as follows: (E) QA, *n* = 289; QAV, *n* = 204; QAL - IPTG, *n* = 205; QAL + IPTG, *n* = 473; and (G) QA, *n* = 499; QAV, *n* = 428; QAL - IPTG, *n* = 534; QAL + IPTG, *n* = 149; QAVJ, *n* = 1334. Scale bars, 5 μm.

interaction with the C-terminal region of FimV (FimV^{C}, aa 481–919), as well as with PilG (Figures 5B and 5C). We further verified that ChpA^{N} interacts with the TPR3 domain of FimV (Figure 5B), consistent with previous reports that FimL binds specifically to TPR3.[19] These results suggest that ChpA^{N} and FimL may associate with overlapping regions of FimV and could therefore compete for FimV binding.

Because ChpA^{N} represents only a portion of the full-length ChpA protein, we further tested whether full-length ChpA also interacts with FimV and PilG. BACTH assays showed that full-length ChpA interacted with both FimV^{C} and PilG (Figures 5B and 5C). However, compared with ChpA^{N}, several positive combinations showed reduced or undetectable activity in the full-length ChpA assays. This difference may reflect conformational constraints, lower expression or stability of the full-length ChpA fusion proteins in the BACTH system, or reduced accessibility of the relevant interaction surfaces in the full-length protein. In addition, the C-terminal region of ChpA (ChpA^{C}, aa 558–2472) produced a detectable BACTH signal with PilG, although the low activity does not by itself provide strong evidence for a robust ChpA^{C}-PilG interaction (Figure 5C). ChpA^{C} showed no detectable binding activity with TPR3 (Figure S18). AlphaFold3 predictions showed that ChpA^{N} and FimL have substantially overlapping predicted binding interfaces on PilG (Table S1), whereas the ChpA^{C}-PilG interaction had a relatively low ipTM score of 0.32, making its binding interface difficult to define with confidence. Therefore, it is currently unresolved whether PilG could simultaneously associate with ChpA^{C} and FimL. Together, these results support an interaction between the N-terminal region of ChpA and PilG, while suggesting that additional regions of ChpA may also contribute to PilG association.

We next examined the subcellular localization of ChpA^{N} and full-length ChpA. Both proteins were expressed as plasmid-encoded sYFP2 fusions. In Δ*pilQ*Δ*chpA* cells, ChpA^{N}-sYFP2 localized to the bacterial poles, whereas deletion of *fimV* disrupted this polar localization (Figures 5D and 5E). Deletion of *fimL* enhanced ChpA^{N} polarity, whereas FimL overexpression reduced ChpA^{N} polar localization (Figures 5D and 5E). These observations are consistent with the idea that FimL negatively affects ChpA^{N} association with FimV, possibly through competition for FimV binding.

Full-length ChpA-sYFP2 showed stronger polar localization than ChpA^{N}-sYFP2 (Figures 5F and 5G). Deletion of *fimV* substantially reduced, but did not completely abolish, the polar localization of full-length ChpA, in contrast to the stronger effect observed for ChpA^{N}. Additional deletion of *pilJ* in the *fimV*-deletion background further weakened ChpA polar localization, although residual polar localization was still observed in a small fraction of cells (Figures 5F and 5G). These results suggest that the polar localization of full-length ChpA is supported by FimV, PilJ, and possibly additional unidentified factors. Similar to ChpA^{N}, full-length ChpA polarity was also sensitive to FimL expression: overexpression of FimL reduced ChpA polar localization to a level close to that observed in the *fimV*-deletion strain (Figures 5F and 5G). Because FimV is a scaffold protein that contributes to the polar localization of multiple other proteins,[18,34,35] deletion of *fimV* may also affect ChpA localization indirectly through downstream components of the FimV-associated polar machinery. Collectively, these data support a model in which ChpA associates with FimV and PilG, while FimL modulates ChpA polar localization, at least in part, by competing with ChpA for association with FimV.

Mechanical compression decreases the apparent distance between ChpA and PilG

Mechanical compression triggered a rapid and reversible adjustment of intracellular cAMP levels within minutes, implying that bacterial mechanotransduction primarily affects protein activity rather than expression. A plausible explanation is that the phosphorylation of PilG was enhanced, thereby stimulating the adenylate cyclase CyaB. We speculated that mechanical compression might decrease the spatial distance between ChpA and PilG, facilitating PilG phosphorylation.

To test this hypothesis, we performed a FLIM-FRET assay by fusing ChpA^{N} to SYFP2[36] and PilG to mScarletI3[37] (Figure 6A). Using the same microfluidic device described in Figure 3E, we applied mechanical compression to bacterial cells and monitored changes in the SYFP2 fluorescence lifetime to assess the relative distance between ChpA^{N} and PilG. Fluorescence lifetimes of polar-localized sYFP2 were extracted for statistical analysis (Figure 6B). In cells expressing ChpA^{N}-sYFP2 alone, the sYFP2 fluorescence lifetime was approximately 2.9 ns, consistent with the intrinsic lifetime of sYFP2 and remained unchanged upon compression (Figure 6C). This control supports that the observed lifetime changes are not simply caused by compression-induced changes in the donor fluorophore or imaging conditions. For the ChpA^{N}-PilG pair, compression decreased the average sYFP2 fluorescence lifetime from 2.69 to 2.56 ns (Figure 6D). Notably, deletion of *fimL* abolished this compression-induced lifetime decrease (Figure 6E). A reduction in donor lifetime was also observed for the ChpA^{N}/FimL FLIM-FRET pair upon compression (Figure 6F). Quantitative analysis revealed that the apparent ChpA-PilG distance decreased from 7.2 ± 1.3 nm to 6.5 ± 1.0 nm upon compression, while the fraction of FRET-participating molecules remained largely unchanged, changing from 0.32 ± 0.12 to 0.36 ± 0.17 (see STAR Methods for calculation details). We also paired full-length ChpA with PilG or FimL to measure compression-induced changes in apparent distance, and obtained results similar to those observed with ChpA^{N} (Figures 6G–6J). These results indicate that mechanical compression decreases the apparent distance between ChpA and PilG in a FimL-dependent manner.

Because ChpA can directly interact with PilG (Figure 5C), the compression-induced decrease in the apparent ChpA-PilG distance observed by FLIM-FRET is not most simply explained as the formation of a new binary ChpA-PilG interaction. One possible explanation is that ChpA and PilG are distributed among multiple FimV-associated subcomplexes at the cell pole, which is consistent with the competitive binding of FimL and ChpA to FimV. Mechanical compression may alter the spatial organization of pre-existing FimV-associated polar complexes. For example, distinct FimV-associated complexes could be brought closer together, thereby decreasing the distance between ChpA and FimL, as well as between ChpA and FimL-associated PilG, as detected by FLIM-FRET (Figure 6). Such spatial

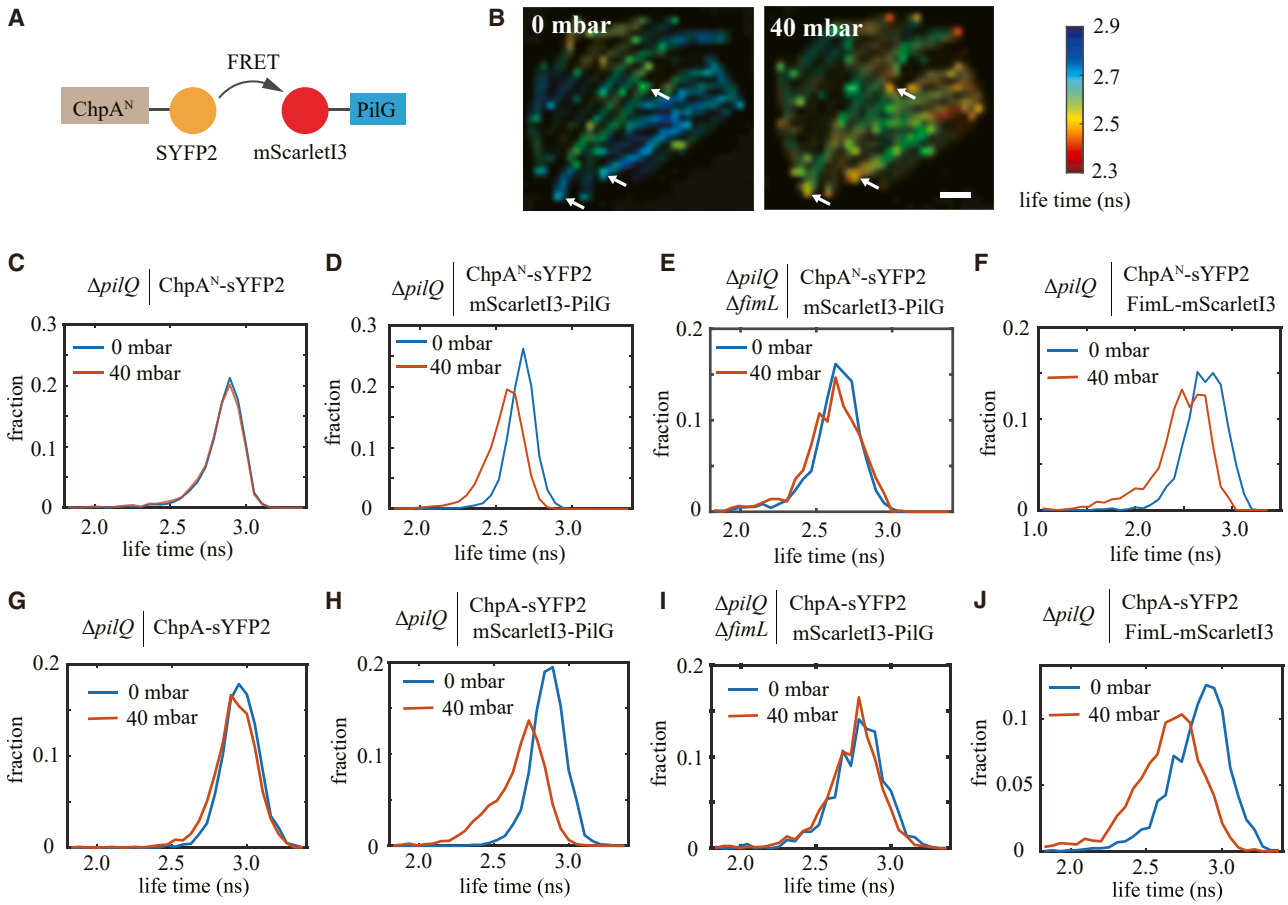


Figure 6. Mechanical compression alters the apparent proximity of ChpA to PilG and FimL

(A) Schematic of the ChpA^N-sYFP2 and mScarletI3-PilG donor-acceptor pair used for FLIM-FRET analysis.

(B) Representative sYFP2 fluorescence lifetime images before (0 mbar) and during (40 mbar) mechanical compression. White arrows indicate polar-localized donor signals used for lifetime analysis. The color scale represents fluorescence lifetime. Scale bars, 1 μm.

(C–F) Fluorescence lifetime distributions for ChpA^N-sYFP2 under the indicated conditions: (C) ChpA^N-sYFP2 alone in Δ*pilQ* cells; (D) ChpA^N-sYFP2 with mScarletI3-PilG in Δ*pilQ* cells; (E) ChpA^N-sYFP2 with mScarletI3-PilG in Δ*pilQ*Δ*fimL* cells; and (F) ChpA^N-sYFP2 with FimL-mScarletI3 in Δ*pilQ* cells.

(G–J) Corresponding fluorescence lifetime distributions using full-length ChpA-sYFP2: (G) ChpA-sYFP2 alone in Δ*pilQ* cells; (H) ChpA-sYFP2 with mScarletI3-PilG in Δ*pilQ* cells; (I) ChpA-sYFP2 with mScarletI3-PilG in Δ*pilQ*Δ*fimL* cells; and (J) ChpA-sYFP2 with FimL-mScarletI3 in Δ*pilQ* cells. Blue and orange curves indicate fluorescence lifetime distributions measured at 0 and 40 mbar, respectively.

The numbers of analyzed bacterial polar regions at 0/40 mbar were as follows: (C) 2007/2335, (D) 355/452, (E) 947/791, (F) 1219/1215, (G) 1256/1671, (H) 1963/2967, (I) 668/856, and (J) 1348/2131. All FLIM-FRET strains additionally lacked the endogenous genes corresponding to the fluorescent fusion proteins; full genotypes are provided in Table S2.

reorganization could increase the local probability of ChpA encountering PilG and promoting PilG phosphorylation, while remaining compatible with the direct ChpA-PilG interaction.

Notably, the Δ*fimL* strain failed to increase cAMP levels upon compression (Figure 4D), and deletion of *fimL* reduced the basal cAMP level to a level close to that observed in the Δ*chpA* and Δ*pilG* strains (Figure 4F). These observations suggest that FimL is unlikely to function solely by competing with ChpA to inhibit PilG phosphorylation. Instead, FimL may help maintain or promote ChpA-dependent PilG signaling, an effect that could be further enhanced by mechanical compression. To further resolve the detailed mechanism, future studies will be needed to quantify the binding affinities among ChpA-PilG and FimL-PilG, determine whether and how FimV undergoes conformational or spatial rearrangement under compression, and clarify how phosphorylated and non-phosphorylated PilG are exchanged among ChpA, FimL, and downstream components such as PilB and CyaB.

To avoid contributions from the corresponding untagged endogenous proteins, all localization and FLIM-FRET experiments were performed using fluorescent protein fusions expressed in strains lacking the corresponding endogenous gene(s) (Table S2). The functionality of the ChpA, FimL, and PilG fusion proteins in these deletion backgrounds was confirmed by measuring intracellular cAMP levels (Figure S19). As noted previously for the localization experiments, the protein-localization and FLIM-FRET measurements were performed using plasmid-expressed fluorescent fusion proteins, including

mScarletI3-PilG, FimL-mScarletI3, and ChpA-sYFP2, rather than fusions expressed from their native chromosomal loci. Plasmid-based expression may result in protein levels that differ from, and potentially exceed, those under native conditions. These results should therefore be interpreted with appropriate caution.

Upregulation of T3SS-associated transcription during compressed-state growth

Having shown that growth-induced mechanical compression increases intracellular cAMP levels, we next investigated whether this response promotes transcription of the T3SS, a well-established downstream output of cAMP-Vfr signaling. In *P. aeruginosa*, cAMP binds the transcription factor Vfr to regulate the expression of multiple genes.[4] The cAMP-Vfr complex directly regulates transcription of *exsA*,[2] which encodes ExsA, the master transcriptional regulator of T3SS gene expression.[38] The T3SS is a critical virulence factor in *P. aeruginosa* infections and plays a particularly important role during acute infection.[39] To examine T3SS-associated transcription during compressed-state growth, we constructed transcriptional reporters in which sfGFP and CyOFP1 were expressed from a selected T3SS promoter and a constitutive promoter, respectively. CyOFP1 fluorescence was used to normalize variations in plasmid copy number and cell density, and the sfGFP/CyOFP1 ratio was used as a measure of T3SS promoter activity.

The observation was conducted in gel microcavities rather than in the microfluidic direct compression device for two reasons. First, T3SS promoter activation occurs downstream of cAMP elevation through a two-step Vfr-cAMP-ExsA-T3SS gene regulatory cascade and therefore requires long-term observation during continued bacterial growth. In the direct compression device, cells are confined between PDMS and glass, and nutrient supply at high cell density mainly depends on lateral diffusion, which limits prolonged imaging after compression. In contrast, the gel microcavity system provides a more suitable environment for sustained growth and long-term monitoring of gene expression. Second, this assay allows us to link the compression-associated cAMP response to downstream transcriptional changes under a growth-induced compression state, rather than only measuring the immediate cAMP response to externally applied pressure.

Promoter activities, normalized by SfGFP/CyOFP1 signals at the onset of single-layer coverage, were visualized using colormaps (Video S7). The majority of T3SS promoters exhibited increased activity 3–4 generations of cell growth post single-layer formation (Figure 7A), corresponding to 1–2 bacterial growth cycles after the cAMP signaling response. 5 generations after single-layer coverage, a 3- to 6-fold increase in average SfGFP/CyOFP1 was observed, while the constitutive promoter J23100 remained unaltered (Figure 7A). Repeating the measurements in the Δ*pilQ*Δ*pilJ*, Δ*pilQ*Δ*lysM*, Δ*pilQ*Δ*pilG*, and Δ*pilQ*Δ*chpA* strains revealed no increase in T3SS promoter activities (Figures 7A and S20). These findings indicate broad upregulation of T3SS-associated promoter activity during compressed-state bacterial growth, subsequent to the mechanically induced cAMP signaling.

DISCUSSION

Our findings demonstrate that mechanical compression triggers cAMP elevation in *P. aeruginosa* through a process we term compression sensing. Notably, the compressive force required to elicit this response (3–30 nN) far exceeds both the tensile force generated by T4Ps (10–200 pN)[40] and the propulsive force produced by the flagellum (0.1–1 pN), yet is comparable to the adhesion force of shear-resistant bacteria in flow (>2 nN).[41] Here, the force refers to the overall load borne by the cell envelope. One key question is: what is the immediate signal following mechanical compression—membrane deformation, peptidoglycan strain, or another stress cue? The peptidoglycan layer warrants particular attention, as FimV contains a LysM motif that binds peptidoglycan, potentially allowing cell-wall deformation to influence the organization of FimV-associated polar complexes. We speculate that mechanical compression may induce conformational or spatial rearrangements involving these complexes, thereby bringing ChpA and PilG into closer proximity and promoting CyaB-dependent cAMP production. However, we currently lack direct evidence for compression-induced conformational changes in FimV. There is still a possibility that the Pil-Chp system itself directly contributes to signal transmission, potentially through PilA-PilJ-mediated coupling.

The spatial heterogeneity of the compression-induced cAMP response likely reflects both mechanical and physiological variability among cells. Although the external load in the microfluidic assay is applied vertically, cell displacement and packing within clusters are expected to redistribute stress and generate additional in-plane forces, such that the local mechanical input experienced by individual cells depends on their position, orientation, and cell-cell contacts. The spatial response patterns observed under sinusoidal compression are consistent with stronger multiaxial confinement near the cluster center and partial stress release toward the periphery. The non-monotonic cAMP dynamics observed in some central cells may therefore reflect a nonlinear dependence on local mechanical load, although stress redistribution, cell rearrangement, adhesive hysteresis, signaling delay, and intrinsic physiological heterogeneity could also contribute. Future experiments that apply quantitatively controlled forces to individual cells will be required to determine how force magnitude and direction influence cAMP.

The comparison between wild-type and Δ*pilQ* cells further suggests that the presence of T4Ps may modulate both the sensitivity and the mechanical context of the compression-induced cAMP response. In gel microcavities, wild-type cells showed an earlier increase in the Gflamp1/CyOFP1 ratio than Δ*pilQ* cells, with cAMP elevation beginning soon after monolayer formation and before the 2-μm-deep cavity was fully occupied (Figures S14A and S14B). This observation suggests that wild-type cells may respond to relatively weak two-dimensional lateral confinement between neighboring cells. However, under direct vertical compression in the microfluidic device, wild-type cells showed a weaker average cAMP response than Δ*pilQ* cells (Figure S13). We speculate that this difference reflects the combined effects of force geometry and T4P-dependent cell movement. Lateral compression between neighboring cells, especially near the cell poles, may be more effective in activating cAMP signaling than

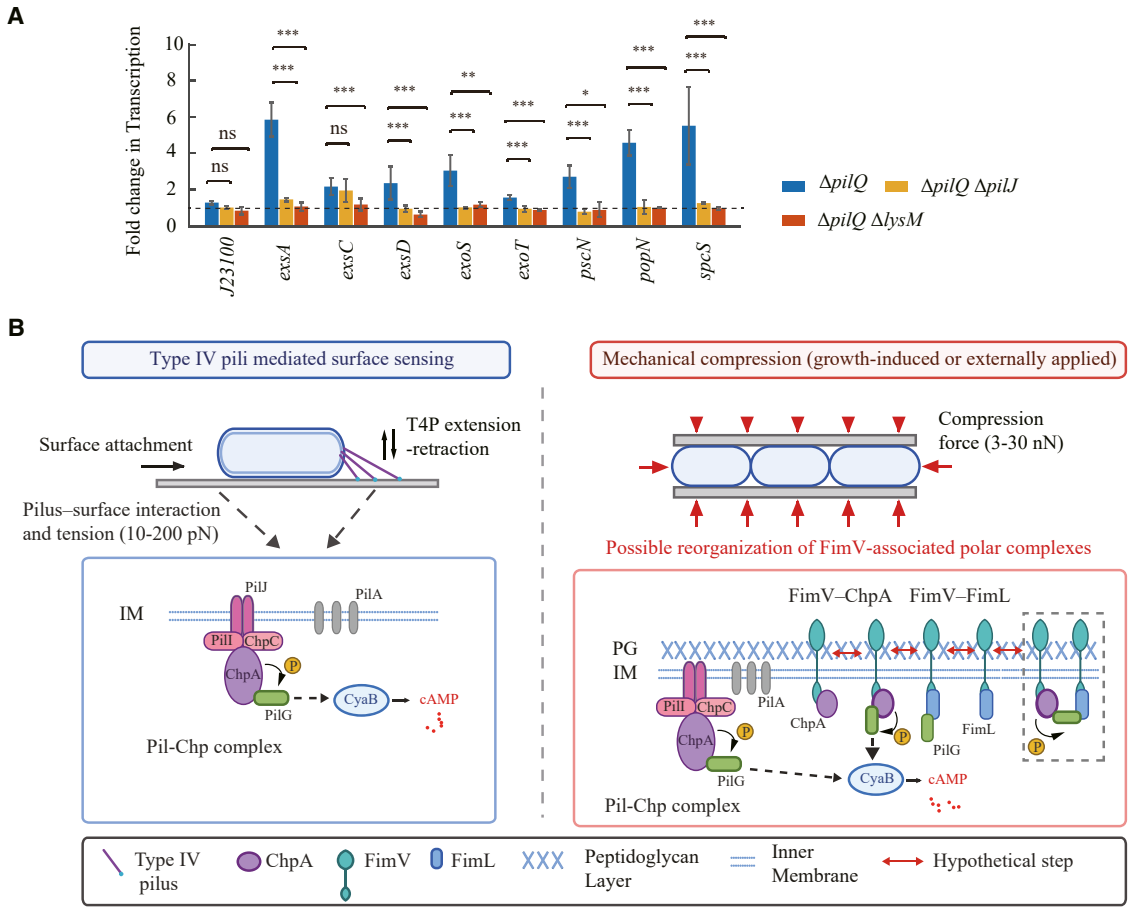


Figure 7. Compression-associated T3SS transcription and proposed working model for mechanical compression-induced cAMP signaling in *P. aeruginosa*

(A) Fold change in type III secretion system (T3SS) promoter expression at 5 generations after monolayer formation relative to that at initial monolayer establishment in Δ*pilQ*, Δ*pilQ*Δ*pilJ*, and Δ*pilQ*Δ*lysM* strains grown in agarose gel microcavities. Sample sizes (microcavities; Δ*pilQ*/Δ*pilQ*Δ*pilJ*/Δ*pilQ*Δ*lysM*) were as follows: J23100, n = 17/6/4; *exsA*, n = 6/2/3; *exsC*, n = 7/4/9; *exsD*, n = 4/2/5; *exoS*, n = 6/7/3; *exoT*, n = 12/5/3; *pscN*, n = 3/5/3; *popN*, n = 4/9/3; and *spcS*, n = 7/4/3. Statistical significance was assessed by t test; ***$p < 0.001$, **$p < 0.01$, *$p < 0.05$; ns, not significant. Data are presented as mean ± SD.

(B) Proposed working model comparing type IV pili-mediated surface sensing with mechanical compression-associated cAMP signaling. In the previously described surface-sensing response (left), type IV pili attach to a surface and undergo extension-retraction cycles, generating pilus-surface interactions and tensile forces. In one proposed model, pilus retraction alters the interaction between membrane-associated PilA and the chemoreceptor PilJ, thereby transmitting mechanical input through the Pil-Chp system, including the PilI/ChpC adapter proteins, ChpA, and PilG, to CyaB-dependent cAMP production. In the mechanical compression-associated response proposed in this study (right), growth-induced crowding or externally applied compression may alter the spatial organization of FimV-associated polar complexes. ChpA and FimL can associate with FimV, and compression may bring these complexes into closer proximity, potentially facilitating interactions among ChpA, PilG, and FimL and thereby promoting PilG-dependent signaling to CyaB. The dashed box illustrates a hypothetical ChpA-PilG-FimL complex in which PilG may associate simultaneously with ChpA and FimL. Red double-headed arrows indicate hypothetical spatial reorganization steps, whereas dashed black arrows indicate proposed signaling connections. The schematic emphasizes the distinct mechanical inputs and potential signaling routes considered here and is not intended to summarize all known branches of surface-sensing regulation.

vertical compression of individual cells. At the same time, T4P-mediated outward movement may partially relieve sustained lateral compression within wild-type cell clusters. Consistent with this idea, wild-type cells frequently moved outward from clusters after pressure release in cyclic compression experiments (Figure S14D), and rapidly exited gel microcavities after cAMP elevation (Figure S14A). Thus, T4Ps may allow wild-type cells to respond to relatively weak lateral confinement under some conditions, while also enabling cells to escape from crowded regions and thereby reduce sustained compression.

These observations may also provide a link to previous studies of twitching motility, in which collisions between cells or with inert obstacles induce directional reversals through Chp-dependent repolarization of motility and signaling proteins, including PilB, FimX, and PilG.[42] Although such reversal-associated polarity changes require functional twitching motility and are mechanistically distinct from the compression response described here, they support the broader idea that the Pil-Chp system can process mechanical inputs during surface-associated growth. Whether transient local compression generated

during cell-cell collisions contributes to Pil-Chp activation during twitching motility remains an open question.

Bacteria commonly inhabit solid surfaces in natural environments. In *P. aeruginosa*, cAMP elevation following surface contact has been identified as a hallmark of surface sensing, mediated by T4Ps through the PilJ-Chp-CyaB pathway[6,7] (Figure 7B). This partially overlaps with the compression sensing mechanism identified here. Notably, the retention of compression-induced cAMP responses in mutants defective in T4P extension or retraction suggests that productive pilus cycling is not itself required for compression sensing. In contrast, PilA remains required. Loss of PilA, as a proposed input for PilJ, may reduce PilJ activity and thereby impair the Pil-Chp system. Currently, whether compression sensing contributes to pilus-mediated surface sensing remains undetermined, as we lack an experimental system that selectively abolishes compression responses while preserving functional T4Ps.

Compression sensing may provide a mechanism for *P. aeruginosa* to activate T3SS within hosts. By responding to mechanical compression, bacteria may preferentially activate virulence-associated programs when the population reaches a sufficiently dense or confined state. Furthermore, compression sensing may enable bacteria to recognize spatially confined colonization sites, such as tissue interstices, triggering appropriate T3SS activation. Another signal activating T3SS is low calcium concentration, which regulates ExsA translation through the LadS/GacS-GacA-RsmYZ-RsmA cascade.[43,44] These two mechanisms may act synergistically in confined environments such as macrophage phagosomes, resulting in robust T3SS expression.

Beyond T3SS activation, compression-induced cAMP signaling may also affect additional Vfr-dependent physiological programs. Vfr is a cAMP-responsive global virulence regulator in *P. aeruginosa* and has been reported to control the expression of more than 200 genes, many of which are associated with virulence and surface adaptation.[3,4,45] Representative Vfr-regulated targets include the quorum-sensing regulator *lasR*, the exotoxin gene *toxA*, and the *fimU-pilVWXY1Y2E* operon.[45–49] Therefore, cAMP elevation during compression may also modulate quorum-sensing responsiveness, toxin-associated virulence programs, and T4P-dependent surface behaviors. In particular, the *fimU-pilVWXY1Y2E* operon encodes minor pilins and PilY1-associated factors that prime T4P assembly and promote PilY1 surface display.[50] Over longer timescales, activation of this operon by cAMP-Vfr may enhance T4P production or remodeling under compression, potentially contributing to the clustered outward movement observed in confined bacterial populations.

From a synthetic biology perspective, compression sensing offers a unique approach to translating mechanical force signals into bacterial phenotypic responses. Bacteria may serve as active materials for sensing mechanical forces, providing information about static stress or stress history. As our understanding deepens, the cAMP response to mechanical force may be fine-tuned, while downstream gene expression can be processed using designed genetic circuits, highlighting the potential to develop novel tools that leverage the interplay between mechanical forces and bacterial physiology.

Limitations of the study

This study identifies mechanical compression as an input that activates cAMP signaling in *Pseudomonas aeruginosa*, but several limitations remain. First, although microfluidic compression and gel microcavity assays provide complementary evidence that compression elevates intracellular cAMP, the local mechanical stress experienced by individual cells from different directions cannot yet be measured directly. The force range reported here is therefore model-dependent and sensitive to assumptions such as bacterial turgor pressure and cell-envelope mechanics.

Second, although our data indicate that CyaB, the Pil-Chp system, and the FimV-FimL module are required for the compression-induced cAMP response, the immediate molecular signal generated by compression remains unresolved. Possible inputs include membrane deformation, peptidoglycan strain, or other envelope-associated stress cues.

Third, FLIM-FRET measurements support compression-dependent proximity changes among ChpA, PilG, and FimL, but these experiments do not directly measure PilG phosphorylation or establish the detailed sequence of molecular events leading to CyaB activation.

Finally, although compressed-state growth upregulates T3SS-associated transcription and may affect broader Vfr-dependent programs, the consequences of compression-induced cAMP signaling during host infection remain to be tested directly in infection models.

RESOURCE AVAILABILITY

Lead contact

Requests for further information, resources, and reagents should be directed to and will be fulfilled by the lead contact, Fan Jin (fan.jin@siat.ac.cn).

Materials availability

Bacterial strains, plasmids, and other newly generated materials reported in this study are available from the lead contact upon reasonable request.

Data and code availability

- The original microscopy data and other data reported in this paper are available from the lead contact upon reasonable request.
- Custom MATLAB code used for image processing, single-cell tracking, and quantitative analysis is publicly available on GitHub and has been archived on Zenodo (https://doi.org/10.5281/zenodo.22095576).
- Other items in this study are available from the lead contact upon reasonable request.

ACKNOWLEDGMENTS

We extend our gratitude to Professor Jun Chu for generously providing the cAMP reporter tool Gflamp1. We thank Jizhou Huang for introducing the Omnipose tool for image processing, Jinjuan Wang for her help in microfluidic device fabrication, and Jialun Lin for his assistance in formatting the manuscript. We thank Haihua Liang's lab for kindly providing tools for the BACTH assay and Xueliang Zhan for his guidance on experimental operation. We thank the Core Facility of Shenzhen Institute of Synthetic Biology (iSynBio Core Facility) for their support in microscopy measurements, especially in the FLIM experiments. This work was supported by the National Key Research and Development Program of China (grant no. 2025YFA0922900 to F.J.), the National Natural Science Foundation of China (grant no. 32101177 to Yajia Huang), National Key Research and Development Program of China (grant no. 2023YFB4605403 to H.L.), and

Shenzhen Engineering Research Center of Therapeutic Synthetic Microbes (grant no. XMHT20220104015 to F.J.).

AUTHOR CONTRIBUTIONS

Postulation of the mechanical compression-dependent cAMP signaling mechanism, F.J.; strain construction, Yajia Huang, L.N., J.X., B.L., and W.X.; initial experimental exploration, Yajia Huang and J.X.; experimental design, F.J., L.N., and Yajia Huang; staining of type IV pili, Yajia Huang; gel microcavity experiment, Yajia Huang and L.N.; microfluidic device design, Y.Y. and S.H.; microfluidic device fabrication, L.N. and H.W.; mechanical compression of bacterial cells in microfluidic device, L.N. and Yajia Huang; gel-glass interface culture experiments, Yajia Huang and L.N.; image processing and data presentation, L.N.; simulation and modeling of forces on bacterial cells, H.L. and Yaoxin Huang; BACTH assay, W.X. and L.N.; FLIM experiment and data analysis, L.N.; manuscript drafting, H.L. and Yaoxin Huang (physical modeling of forces acting on bacteria); L.N. (remaining content), F.J., L.N., H.L., Yajia Huang, and Yaoxin Huang.

DECLARATION OF INTERESTS

The authors declare no competing interests.

DECLARATION OF GENERATIVE AI AND AI-ASSISTED TECHNOLOGIES IN THE MANUSCRIPT PREPARATION PROCESS

During the preparation of this work, the authors used ChatGPT (OpenAI) for language editing, improving clarity, and readability. The authors reviewed and edited all AI-assisted output as needed and take full responsibility for the content of the published article.

STAR★METHODS

Detailed methods are provided in the online version of this paper and include the following:

- KEY RESOURCES TABLE
- EXPERIMENTAL MODEL AND STUDY PARTICIPANT DETAILS
  - Bacterial strains and growth conditions
- METHOD DETAILS
  - Fabrication of molds for the gel microcavity assay
  - Fabrication of the microfluidic direct-compression device
  - Gel–glass interface assay
  - Gel microcavity assay
  - Fluorescence imaging of gel-based assays
  - Particle image velocimetry analysis
  - Direct mechanical compression in the microfluidic device
  - Fluorescence imaging and single-cell analysis in the microfluidic compression assay
  - Finite-element estimation of mechanical stress in gel microcavities
  - Estimation of mechanical force in the microfluidic direct-compression assay
  - Bacterial adenylate cyclase two-hybrid assay
  - Fluorescence lifetime imaging microscopy
  - Estimation of apparent donor–acceptor distance from FLIM measurements
- QUANTIFICATION AND STATISTICAL ANALYSIS

SUPPLEMENTAL INFORMATION

Supplementary data related to this article can be found online at https://doi.org/10.1016/j.celrep.2026.118114.

Received: March 4, 2026
Revised: July 18, 2026
Accepted: September 21, 2026

REFERENCES

1. Horna, G., and Ruiz, J. (2021). Type 3 secretion system of *Pseudomonas aeruginosa*. Microbiol. Res. *246*, 126719. https://doi.org/10.1016/j.micres.2021.126719.
2. Marsden, A.E., Intile, P.J., Schulmeyer, K.H., Simmons-Patterson, E.R., Urbanowski, M.L., Wolfgang, M.C., and Yahr, T.L. (2016). Vfr directly activates *exsA* transcription to regulate expression of the *Pseudomonas aeruginosa* type III secretion system. J. Bacteriol. *198*, 1442–1450. https://doi.org/10.1128/JB.00049-16.
3. Wolfgang, M.C., Lee, V.T., Gilmore, M.E., and Lory, S. (2003). Coordinate regulation of bacterial virulence genes by a novel adenylate cyclase-dependent signaling pathway. Dev. Cell *4*, 253–263. https://doi.org/10.1016/S1534-5807(03)00019-4.
4. Fuchs, E.L., Brutinel, E.D., Klem, E.R., Fehr, A.R., Yahr, T.L., and Wolfgang, M.C. (2010). *In vitro* and *in vivo* characterization of the *Pseudomonas aeruginosa* cyclic AMP (cAMP) phosphodiesterase CpdA, required for cAMP homeostasis and virulence factor regulation. J. Bacteriol. *192*, 2779–2790. https://doi.org/10.1128/jb.00168-10.
5. Fulcher, N.B., Holliday, P.M., Klem, E., Cann, M.J., and Wolfgang, M.C. (2010). The *Pseudomonas aeruginosa* Chp chemosensory system regulates intracellular cAMP levels by modulating adenylate cyclase activity. Mol. Microbiol. *76*, 889–904. https://doi.org/10.1111/j.1365-2958.2010.07135.x.
6. Persat, A., Inclan, Y.F., Engel, J.N., Stone, H.A., and Gitai, Z. (2015). Type IV pili mechanochemically regulate virulence factors in *Pseudomonas aeruginosa*. Proc. Natl. Acad. Sci. USA *112*, 7563–7568. https://doi.org/10.1073/pnas.1502025112.
7. Luo, Y., Zhao, K., Baker, A.E., Kuchma, S.L., Coggan, K.A., Wolfgang, M.C., Wong, G.C.L., and O'Toole, G.A. (2015). A hierarchical cascade of second messengers regulates *Pseudomonas aeruginosa* surface behaviors. mBio *6*, e02456-14. https://doi.org/10.1128/mbio.02456-14.
8. Burrows, L.L. (2012). *Pseudomonas aeruginosa* twitching motility: Type IV pili in action. Annu. Rev. Microbiol. *66*, 493–520. https://doi.org/10.1146/annurev-micro-092611-150055.
9. Silversmith, R.E., Wang, B., Fulcher, N.B., Wolfgang, M.C., and Bourret, R.B. (2016). Phosphoryl group flow within the *Pseudomonas aeruginosa* Pil-Chp chemosensory system: Differential function of the eight phosphotransferase and three receiver domains. J. Biol. Chem. *291*, 17677–17691. https://doi.org/10.1074/jbc.M116.737528.
10. Kühn, M.J., Macmillan, H., Talà, L., Inclan, Y., Patino, R., Pierrat, X., Al-Mayyah, Z., Engel, J.N., and Persat, A. (2023). Two antagonistic response regulators control *Pseudomonas aeruginosa* polarization during mechanotaxis. EMBO J. *42*, 112165. https://doi.org/10.15252/embj.2022112165.
11. Koch, M.D., Black, M.E., Han, E., Shaevitz, J.W., and Gitai, Z. (2022). *Pseudomonas aeruginosa* distinguishes surfaces by stiffness using retraction of type IV pili. Proc. Natl. Acad. Sci. USA *119*, 2119434119. https://doi.org/10.1073/pnas.2119434119.
12. Geiger, C.J., and O'Toole, G.A. (2023). Evidence for the type IV pilus retraction motor PilT as a component of the surface sensing system in *Pseudomonas aeruginosa*. J. Bacteriol. *205*, 00179. https://doi.org/10.1128/jb.00179-23.
13. Patino, R., Kühn, M.J., Macmillan, H., Inclan, Y.F., Chavez, I., Persat, A., and Engel, J.N. (2025). Antagonistic response regulators spatially regulate receptor methylation in the *Pseudomonas aeruginosa* pil–chp surface sensing system. Cell Rep. *44*, 115536. https://doi.org/10.1016/j.celrep.2025.115536.
14. Oliveira, N.M., Foster, K.R., and Durham, W.M. (2016). Single-cell twitching chemotaxis in developing biofilms. Proc. Natl. Acad. Sci. USA *113*, 6532–6537. https://doi.org/10.1073/pnas.1600760113.
15. Yarrington, K.D., Shendruk, T.N., and Limoli, D.H. (2024). The type IV pilus chemoreceptor PilJ controls chemotaxis of one bacterial species towards another. PLoS Biol. *22*, 3002488. https://doi.org/10.1371/journal.pbio.3002488.

16. Wheeler, J.H.R., Foster, K.R., and Durham, W.M. (2024). Individual bacterial cells can use spatial sensing of chemical gradients to direct chemotaxis on surfaces. Nat. Microbiol. *9*, 2308–2322. https://doi.org/10.1038/s41564-024-01729-3.

17. Inclan, Y.F., Persat, A., Greninger, A., Von Dollen, J., Johnson, J., Krogan, N., Gitai, Z., and Engel, J.N. (2016). A scaffold protein connects type IV pili with the Chp chemosensory system to mediate activation of virulence signaling in *Pseudomonas aeruginosa*. Mol. Microbiol. *101*, 590–605. https://doi.org/10.1111/mmi.13410.

18. Buensuceso, R.N.C., Daniel-Ivad, M., Kilmury, S.L.N., Leighton, T.L., Harvey, H., Howell, P.L., and Burrows, L.L. (2017). Cyclic AMP-independent control of twitching motility in *Pseudomonas aeruginosa*. J. Bacteriol. *199*, 00188. https://doi.org/10.1128/jb.00188-17.

19. Buensuceso, R.N.C., Nguyen, Y., Zhang, K., Daniel-Ivad, M., Sugiman-Marangos, S.N., Fleetwood, A.D., Zhulin, I.B., Junop, M.S., Howell, P.L., and Burrows, L.L. (2016). The conserved tetratricopeptide repeat-containing C-terminal domain of *Pseudomonas aeruginosa* FimV is required for its cyclic AMP-dependent and -independent functions. J. Bacteriol. *198*, 2263–2274. https://doi.org/10.1128/jb.00322-16.

20. Webster, S.S., Lee, C.K., Schmidt, W.C., Wong, G.C.L., and O'Toole, G.A. (2021). Interaction between the type 4 pili machinery and a diguanylate cyclase fine-tune c-di-GMP levels during early biofilm formation. Proc. Natl. Acad. Sci. USA *118*, 2105566118. https://doi.org/10.1073/pnas.2105566118.

21. Webster, S.S., Mathelié-Guinlet, M., Verissimo, A.F., Schultz, D., Viljoen, A., Lee, C.K., Schmidt, W.C., Wong, G.C.L., Dufrêne, Y.F., and O'Toole, G.A. (2022). Force-induced changes of PilY1 drive surface sensing by *Pseudomonas aeruginosa*. mBio *13*, e03754-21. https://doi.org/10.1128/mbio.03754-21.

22. Cao-Garcia, F.J., Walker, J.E., Board, S., and Alonso-Caballero, A. (2025). Mechanical forces and ligand binding modulate *Pseudomonas aeruginosa* PilY1 mechanosensitive protein. Life Sci. Alliance *8*, 202403111. https://doi.org/10.26508/lsa.202403111.

23. Wang, L., Wu, C., Peng, W., Zhou, Z., Zeng, J., Li, X., Yang, Y., Yu, S., Zou, Y., Huang, M., et al. (2022). A high-performance genetically encoded fluorescent indicator for *in vivo* cAMP imaging. Nat. Commun. *13*, 5363. https://doi.org/10.1038/s41467-022-32994-7.

24. Chu, J., Oh, Y., Sens, A., Ataie, N., Dana, H., Macklin, J.J., Laviv, T., Welf, E.S., Dean, K.M., Zhang, F., et al. (2016). A bright cyan-excitable orange fluorescent protein facilitates dual-emission microscopy and enhances bioluminescence imaging *in vivo*. Nat. Biotechnol. *34*, 760–767. https://doi.org/10.1038/nbt.3550.

25. Altieri, S.L., Clayton, G.M., Silverman, W.R., Olivares, A.O., De la Cruz, E.M., Thomas, L.R., and Morais-Cabral, J.H. (2008). Structural and energetic analysis of activation by a cyclic nucleotide binding domain. J. Mol. Biol. *381*, 655–669. https://doi.org/10.1016/j.jmb.2008.06.011.

26. Zheng, X., Gomez-Rivas, E.J., Lamont, S.I., Daneshjoo, K., Shieh, A., Wozniak, D.J., and Parsek, M.R. (2024). The surface interface and swimming motility influence surface-sensing responses in *Pseudomonas aeruginosa*. Proc. Natl. Acad. Sci. USA *121*, 2411981121. https://doi.org/10.1073/pnas.2411981121.

27. Delarue, M., Hartung, J., Schreck, C., Gniewek, P., Hu, L., Herminghaus, S., and Hallatschek, O. (2016). Self-driven jamming in growing microbial populations. Nat. Phys. *12*, 762–766. https://doi.org/10.1038/nphys3741.

28. Anyan, M.E., Amiri, A., Harvey, C.W., Tierra, G., Morales-Soto, N., Driscoll, C.M., Alber, M.S., and Shrout, J.D. (2014). Type IV pili interactions promote intercellular association and moderate swarming of *Pseudomonas aeruginosa*. Proc. Natl. Acad. Sci. USA *111*, 18013–18018. https://doi.org/10.1073/pnas.1414661111.

29. Normand, V., Lootens, D.L., Amici, E., Plucknett, K.P., and Aymard, P. (2000). New insight into agarose gel mechanical properties. Biomacromolecules *1*, 730–738. https://doi.org/10.1021/bm005583j.

30. Vella, D., Ajdari, A., Vaziri, A., and Boudaoud, A. (2012). Indentation of ellipsoidal and cylindrical elastic shells. Phys. Rev. Lett. *109*, 144302. https://doi.org/10.1103/PhysRevLett.109.144302.

31. Wehbi, H., Portillo, E., Harvey, H., Shimkoff, A.E., Scheurwater, E.M., Howell, P.L., and Burrows, L.L. (2011). The peptidoglycan-binding protein fimv promotes assembly of the pseudomonas aeruginosa type iv pilus secretin. J. Bacteriol. *193*, 540–550. https://doi.org/10.1128/JB.01048-10.

32. Alon, U., Surette, M.G., Barkai, N., and Leibler, S. (1999). Robustness in bacterial chemotaxis. Nature *397*, 168–171. https://doi.org/10.1038/16483.

33. Whitchurch, C.B., Leech, A.J., Young, M.D., Kennedy, D., Sargent, J.L., Bertrand, J.J., Semmler, A.B.T., Mellick, A.S., Martin, P.R., Alm, R.A., et al. (2004). Characterization of a complex chemosensory signal transduction system which controls twitching motility in *Pseudomonas aeruginosa*. Mol. Microbiol. *52*, 873–893. https://doi.org/10.1111/j.1365-2958.2004.04026.x.

34. Nicastro, G.G., Kaihami, G.H., Pulschen, A.A., Hernandez-Montelongo, J., Boechat, A.L., de Oliveira Pereira, T., Rosa, C.G.T., Stefanello, E., Colepicolo, P., Bordi, C., and Baldini, R.L. (2020). c-di-gmp-related phenotypes are modulated by the interaction between a diguanylate cyclase and a polar hub protein. Sci. Rep. *10*, 3077. https://doi.org/10.1038/s41598-020-59536-9.

35. Carter, T., Buensuceso, R.N.C., Tammam, S., Lamers, R.P., Harvey, H., Howell, P.L., and Burrows, L.L. (2017). The type iva pilus machinery is recruited to sites of future cell division. mBio *8*, e02103-16–02116. https://doi.org/10.1128/mBio.02103-16.

36. Kremers, G.-J., Goedhart, J., van Munster, E.B., Jr., and Gadella, T.W.J. (2006). Cyan and yellow super fluorescent proteins with improved brightness, protein folding, and FRET Förster radius. Biochemistry *45*, 6570–6580. https://doi.org/10.1021/bi0516273.

37. Gadella, T.W.J., Jr, van Weeren, L., Stouthamer, J., Hink, M.A., Wolters, A.H.G., Giepmans, B.N.G., Aumonier, S., Dupuy, J., and Royant, A. (2023). mScarlet3: A brilliant and fast-maturing red fluorescent protein. Nat. Methods *20*, 541–545. https://doi.org/10.1038/s41592-023-01809-y.

38. Yahr, T.L., and Wolfgang, M.C. (2006). Transcriptional regulation of the *Pseudomonas aeruginosa* type III secretion system. Mol. Microbiol. *62*, 631–640. https://doi.org/10.1111/j.1365-2958.2006.05412.x.

39. Hauser, A.R. (2009). The type III secretion system of *Pseudomonas aeruginosa*: Infection by injection. Nat. Rev. Microbiol. *7*, 654–665. https://doi.org/10.1038/nrmicro2199.

40. Maier, B., Potter, L., So, M., Seifert, H.S., Sheetz, M.P., and Sheetz, M.P. (2002). Single pilus motor forces exceed 100 pN. Proc. Natl. Acad. Sci. USA *99*, 16012–16017. https://doi.org/10.1073/pnas.242523299.

41. Zhang, R., Xia, A., Ni, L., Li, F., Jin, Z., Yang, S., and Jin, F. (2017). Strong shear flow persister bacteria resist mechanical washings on the surfaces of various polymer materials. Adv. Biosyst. *1*, 1700161. https://doi.org/10.1002/adbi.201700161.

42. Kühn, M.J., Talà, L., Inclan, Y.F., Patino, R., Pierrat, X., Vos, I., Al-Mayyah, Z., Macmillan, H., Negrete, J., Engel, J.N., and Persat, A. (2021). Mechanotaxis directs *Pseudomonas aeruginosa* twitching motility. Proc. Natl. Acad. Sci. USA *118*, 2101759118. https://doi.org/10.1073/pnas.2101759118.

43. Broder, U.N., Jaeger, T., and Jenal, U. (2016). LadS is a calcium-responsive kinase that induces acute-to-chronic virulence switch in *Pseudomonas aeruginosa*. Nat. Microbiol. *2*, 16184. https://doi.org/10.1038/nmicrobiol.2016.184.

44. Brencic, A., and Lory, S. (2009). Determination of the regulon and identification of novel mRNA targets of *Pseudomonas aeruginosa* RsmA. Mol. Microbiol. *72*, 612–632. https://doi.org/10.1111/j.1365-2958.2009.06670.x.

45. Coggan, K.A., Higgs, M.G., Brutinel, E.D., Marden, J.N., Intile, P.J., Winther-Larsen, H.C., Koomey, M., Yahr, T.L., and Wolfgang, M.C. (2022). Global regulatory pathways converge to control expression of Pseudomonas aeruginosa type IV pili. mBio *13*, e03696-21–21. https://doi.org/10.1128/mbio.03696-21.

46. Albus, A.M., Pesci, E.C., Runyen-Janecky, L.J., West, S.E., and Iglewski, B.H. (1997). Vfr controls quorum sensing in Pseudomonas aeruginosa. J. Bacteriol. *179*, 3928–3935. https://doi.org/10.1128/jb.179.12.3928-3935.1997.

47. West, S.E., Sample, A.K., and Runyen-Janecky, L.J. (1994). The *vfr* gene product, required for Pseudomonas aeruginosa exotoxin A and protease production, belongs to the cyclic AMP receptor protein family. J. Bacteriol. *176*, 7532–7542. https://doi.org/10.1128/jb.176.24.7532-7542.1994.

48. Davinic, M., Carty, N.L., Colmer-Hamood, J.A., San Francisco, M., and Hamood, A.N. (2009). Role of Vfr in regulating exotoxin A production by Pseudomonas aeruginosa. Microbiology *155*, 2265–2273. https://doi.org/10.1099/mic.0.028373-0.

49. Belete, B., Lu, H., and Wozniak, D.J. (2008). Pseudomonas aeruginosa AlgR regulates type IV pilus biosynthesis by activating transcription of the *fimU-pilVWXY1Y2E* operon. J. Bacteriol. *190*, 2023–2030. https://doi.org/10.1128/JB.01623-07.

50. Nguyen, Y., Sugiman-Marangos, S., Harvey, H., Bell, S.D., Charlton, C.L., Junop, M.S., and Burrows, L.L. (2015). Pseudomonas aeruginosa minor pilins prime type IVa pilus assembly and promote surface display of the PilY1 adhesin. J. Biol. Chem. *290*, 601–611. https://doi.org/10.1074/jbc.M114.616904.

51. Heydorn, A., Nielsen, A.T., Hentzer, M., Sternberg, C., Givskov, M., Ersbøll, B.K., and Molin, S. (2000). Quantification of biofilm structures by the novel computer program COMSTAT. Microbiology *146*, 2395–2407. https://doi.org/10.1099/00221287-146-10-2395.

52. Chen, W., Zhang, J., Li, F., Wang, C., Zhang, Y., Xia, A., Ni, L., and Jin, F. (2022). Genome-wide analysis of gene expression noise brought about by transcriptional regulation in *Pseudomonas aeruginosa*. mSystems *7*, e00963-22. https://doi.org/10.1128/msystems.00963-22.

53. Thielicke, W., and Sonntag, R. (2021). Particle image velocimetry for MATLAB: Accuracy and enhanced algorithms in PIVlab. J. Open Res. Softw. *9*, 12. https://doi.org/10.5334/jors.334.

54. Cutler, K.J., Stringer, C., Lo, T.W., Rappez, L., Stroustrup, N., Brook Peterson, S., Wiggins, P.A., Mougous, J.D., Keegstra, J.M., Soifer, I., et al. (2022). Omnipose: a high-precision morphology-independent solution for bacterial cell segmentation. Nat. Methods *19*, 1438–1448. https://doi.org/10.1038/s41592-022-01639-4.

55. Hong, W., Zhao, X., Zhou, J., and Suo, Z. (2008). A theory of coupled diffusion and large deformation in polymeric gels. J. Mech. Phys. Solids *56*, 1779–1793. https://doi.org/10.1016/j.jmps.2007.11.010.

56. Wang, X., and Hong, W. (2012). A visco-poroelastic theory for polymeric gels. Proc. R. Soc. A A. *468*, 3824–3841. https://doi.org/10.1098/rspa.2012.0385.

57. Yao, X., Jericho, M., Pink, D., and Beveridge, T. (1999). Thickness and elasticity of gram-negative murein sacculi measured by atomic force microscopy. J. Bacteriol. *181*, 6865–6875. https://doi.org/10.1128/JB.181.22.6865-6875.1999.

58. Tuson, H.H., Auer, G.K., Renner, L.D., Hasebe, M., Tropini, C., Salick, M., Crone, W.C., Gopinathan, A., Huang, K.C., and Weibel, D.B. (2012). Measuring the stiffness of bacterial cells from growth rates in hydrogels of tunable elasticity. Mol. Microbiol. *84*, 874–891. https://doi.org/10.1111/j.1365-2958.2012.08063.x.

59. Lee, J., Jha, K., Harper, C.E., Zhang, W., Ramsukh, M., Bouklas, N., Dörr, T., Chen, P., and Hernandez, C.J. (2024). Determining the young's modulus of the bacterial cell envelope. ACS Biomater. Sci. Eng. *10*, 2956–2966. https://doi.org/10.1021/acsbiomaterials.4c00105.

60. Nanninga, N., and Woldringh, C.L. (1985). Cell growth, genome duplication, and cell division. In Molecular Cytology of Escherichia Coli, N. Nanninga, ed. (Academic Press), pp. 259–318.

61. Scott Cayley, D., Guttman, H.J., and Thomas Record, M., Jr. (2000). Biophysical characterization of changes in amounts and activity of *Escherichia coli* cell and compartment water and turgor pressure in response to osmotic stress. Biophys. J. *78*, 1748–1764. https://doi.org/10.1016/S0006-3495(00)76726-9.

62. Karimova, G., Pidoux, J., Ullmann, A., and Ladant, D. (1998). A bacterial two-hybrid system based on a reconstituted signal transduction pathway. Proc. Natl. Acad. Sci. USA *95*, 5752–5756. https://doi.org/10.1073/pnas.95.10.5752.

STAR★METHODS

KEY RESOURCES TABLE

REAGENT or RESOURCE	SOURCE	IDENTIFIER
Bacterial strains		
Pseudomonas aeruginosa PAO1	J. D. Shrout	Table S2
PAO1 Δ*cyaA*	This study	Table S2
PAO1 Δ*cyaB*	This study	Table S2
PAO1 Δ*pilQ*	This study	Table S2
PAO1 Δ*pilA*	This study	Table S2
PAO1 Δ*pilB*	This study	Table S2
PAO1 Δ*pilT*	This study	Table S2
PAO1 Δ*pilY1*	This study	Table S2
PAO1 Δ*pilQ* Δ*cyaA*	This study	Table S2
PAO1 Δ*pilQ* Δ*cyaB*	This study	Table S2
PAO1 Δ*pilQ* Δ*fliC*	This study	Table S2
PAO1 Δ*pilQ* Δ*pilG*	This study	Table S2
PAO1 Δ*pilQ* Δ*pilJ*	This study	Table S2
PAO1 Δ*pilQ* Δ*chpA*	This study	Table S2
PAO1 Δ*pilQ* Δ*fimL*	This study	Table S2
PAO1 Δ*pilQ* Δ*fimV*	This study	Table S2
PAO1 Δ*pilQ* Δ*lysM*	This study	Table S2
Strains for FLIM analysis		
PAO1 Δ*pilQ* Δ*chpA* Δ*pilG*::PfimV-*fimV*-ctx2/mScarletI3-*pilG*-PpilJ-*chpA*^{N}-*syfp2*	This study	Table S2
PAO1 Δ*pilQ* Δ*chpA* Δ*pilG*::PfimV-*fimV*-ctx2/mScarletI3-*pilG*-PpilJ-*chpA*-*syfp2*	This study	Table S2
PAO1 Δ*pilQ* Δ*chpA* Δ*pilG* Δ*fimL*::PfimV-*fimV*-ctx2/mScarletI3-*pilG*-PpilJ-*chpA*^{N}-*syfp2*	This study	Table S2
PAO1 Δ*pilQ* Δ*chpA* Δ*pilG* Δ*fimL*::PfimV-*fimV*-ctx2/mScarletI3-*pilG*-PpilJ-*chpA*-*syfp2*	This study	Table S2
PAO1 Δ*pilQ* Δ*chpA* Δ*fimL*/*fimL*-mScarletI3-PpilJ-RBSII-*chpA*^{N}-*syfp2*	This study	Table S2
PAO1 Δ*pilQ* Δ*chpA* Δ*fimL*::PfimV-*fimV*-ctx2/*fimL*-mScarletI3-PpilJ-RBSII-*chpA*-*syfp2*	This study	Table S2
PAO1 Δ*pilQ* Δ*chpA* Δ*fimL*/*chpA*^{N}-*syfp2*	This study	Table S2
PAO1 Δ*pilQ* Δ*chpA* Δ*fimL*/*chpA*-*syfp2*	This study	Table S2
Strains for ChpA^{N} *or ChpA subcellular localization analysis*		
PAO1 Δ*pilQ* Δ*chpA*/*chpA*^{N}-*syfp2*	This study	Table S2
PAO1 Δ*pilQ* Δ*chpA*/*chpA*-*syfp2*	This study	Table S2
PAO1 Δ*pilQ* Δ*chpA* Δ*fimL*/*chpA*^{N}-*syfp2*	This study	Table S2
PAO1 Δ*pilQ* Δ*chpA* Δ*fimL*/*chpA*-*syfp2*	This study	Table S2
PAO1 Δ*pilQ* Δ*chpA* Δ*fimV*/*chpA*^{N}-*syfp2*	This study	Table S2
PAO1 Δ*pilQ* Δ*chpA* Δ*fimV*/*chpA*-*syfp2*	This study	Table S2
PAO1 Δ*pilQ* Δ*chpA* Δ*fimL*::PA1O4O3-*fimL*-ctx2/*chpA*^{N}-*syfp2*	This study	Table S2
PAO1 Δ*pilQ* Δ*chpA* Δ*fimL*::PA1O4O3-*fimL*-ctx2/*chpA*-*syfp2*	This study	Table S2
Escherichia coli Top10	Invitrogen	Table S2
Plasmids		
Gflamp1 plasmid	This study	Table S2
transcriptional reporter plasmids	This study	Table S2

(*Continued on next page*)

Continued

REAGENT or RESOURCE	SOURCE	IDENTIFIER
BACTH plasmids	This study	Table S2
pCasPA, pACRISPR plasmids	This study	Available upon reasonable request
Critical commercial assays		
Bacterial adenylate cyclase two-hybrid system	Euromedex	BACTH kit
Deposited data		
Raw microscopy images	This study	Available upon reasonable request
Custom MATLAB scripts	This study	Zenodo: https://doi.org/10.5281/zenodo.22095576
Software and algorithms		
MATLAB	MathWorks	Used for image processing and analysis
PIVlab	Thielicke and Sonntag	MATLAB toolbox, version 3.09
Omnipose	Cutler et al.	"bact fluor omni" model
COMSOL Multiphysics	COMSOL	Version 6.0
SPCImage	Becker & Hickl GmbH	Version 8.9 NG
Custom MATLAB scripts	This study	Zenodo https://doi.org/10.5281/zenodo.22095576
Other		
Olympus IX83 inverted fluorescence microscope	Olympus	Gel–glass and microcavity imaging
Leica MM165 spinning-disk confocal microscope	Leica	Microfluidic compression imaging
Nikon Eclipse Ti2 inverted confocal microscope	Nikon	FLIM imaging
Photometrics BSI cameras	Photometrics	Dual-camera fluorescence imaging
FluidicLab PC-1 pressure controller	FluidicLab	Microfluidic compression
HPM-100–40 hybrid PMT	Becker & Hickl	FLIM detector
SPC-150N TCSPC module	Becker & Hickl	Photon counting
515 nm pulsed laser	Becker & Hickl/LHB-104	FLIM excitation

EXPERIMENTAL MODEL AND STUDY PARTICIPANT DETAILS

Bacterial strains and growth conditions

Bacterial strains and plasmids used in this study are listed in Table S2. Unless otherwise specified, all bacterial cultures used for microscopy experiments were prepared using a two-step culture procedure at 37°C. Bacteria were first scraped from overnight agar plates and cultured overnight with shaking. The overnight cultures were then diluted 50-fold and cultured with shaking for approximately 6 h until they reached an OD_{600} of approximately 0.5. Unless otherwise specified, bacteria were cultured in FAB medium[51] supplemented with 30 mM sodium glutamate and 30 μg/mL gentamicin (FABG).

For the co-culture experiments, *Escherichia coli* and *Pseudomonas aeruginosa* were cultured separately overnight with shaking in 1 mL M9 medium supplemented with 2% casamino acids and 30 μg/mL gentamicin (M9CAG) at 37°C. Each overnight culture was diluted 100-fold into fresh M9CAG and grown at 37°C to an OD_{600} of approximately 0.5.

METHOD DETAILS

Detail methods for strain construction, type IV pili staining, protein purification, simulation and modeling of bacterial compression stress are included in the Supplemental Information.

Fabrication of molds for the gel microcavity assay

Polydimethylsiloxane (PDMS; Sylgard 184, Dow Corning) structures were fabricated using standard soft-lithography procedures. Silicon wafers were coated with SU-8 2010 photoresist (MicroChem) and patterned to generate an array of cylindrical cavities 30 μm in diameter and 2 μm in height. PDMS prepolymer and curing agent were mixed at a 10:1 mass ratio, poured over the patterned wafer, and cured at 80°C for 1 h. A 14 mm $\times$ 10 mm PDMS block was excised from the cured layer. The lower surface of this block contained cylindrical protrusions corresponding to the patterned cavities and was used as the mold for preparing agarose gel microcavities.

Fabrication of the microfluidic direct-compression device

The air-layer wafer was fabricated using SU-8 2010 photoresist to generate a 20-μm-thick patterned layer. The liquid-layer wafer contained two photoresist layers. The first layer was fabricated using SU-8 6002 to produce an approximately 3.5-μm-thick film corresponding to the red square regions in Figure S7. This layer generated 3.5-μm-high square protrusions on the mold. The second layer was fabricated using SU-8 2010 to produce an 18-μm-thick film corresponding to the black-line regions in Figure S7, in which the square compression pillars and circular support pillars were represented by recessed features. The resulting compression pillars were 14.5 μm high, whereas the support pillars were 18 μm high. This geometry generated a 3.5-μm gap between the compression pillars and the bottom coverslip and prevented the compression pillars from adhering to the glass during plasma bonding. Photolithography was performed according to the manufacturers' instructions for the respective photoresists.

The upper air-layer component was prepared by mixing PDMS prepolymer and curing agent at a 10:1 mass ratio (20 g and 2 g, respectively), pouring the mixture onto the air-layer mold, and curing it at 80°C for 1 h. The cured PDMS was cut into individual chips and access ports were punched.

The thin liquid-layer membrane was prepared by mixing PDMS prepolymer and curing agent at a 9:1 mass ratio (9 g and 1 g, respectively), pouring the mixture onto the liquid-layer wafer, spin-coating at 800 rpm for 30 s, and curing it on a level heating platform at 80°C for 1 h.

The upper-layer chips and the PDMS membrane, while the membrane remained on the liquid-layer wafer, were plasma-treated for 50 s. Methanol (100 μL) was added onto the membrane to facilitate alignment, and the upper-layer chip was immediately positioned under an optical microscope such that the square pillars in the membrane were aligned with the central regions of the square chambers in the upper layer. Methanol was allowed to evaporate for 15 min. The assembly was then placed under vacuum for 3 min and baked at 80°C for 2 h. The assembled chip was peeled from the wafer, and access ports were punched. The outer surface of the membrane was then bonded to a 24 mm $\times$ 50 mm, 0.17-mm-thick coverslip after plasma treatment for 50 s, followed by baking at 80°C for 1 h.

Gel–glass interface assay

Bacterial cultures at an OD_{600} of approximately 0.5 were diluted 50-fold in fresh FABG. A 2 μL aliquot of the diluted bacterial suspension was deposited onto a 1.5% agarose gel pad prepared with FABG. After air-drying, the gel pad was inverted and placed in a round glass-bottom culture dish.

For bacterial co-culture experiments, independently cultured *E. coli* and *P. aeruginosa* suspensions at an OD_{600} of approximately 0.5 were harvested and mixed at a 10:1 ratio (*E. coli*:*P. aeruginosa*). A 2 μL aliquot of the mixture was deposited onto a 1.5% agarose gel pad prepared with M9CAG. After air-drying, the gel pad was inverted and placed in a glass-bottom dish.

Gel microcavity assay

Gel microcavity samples were prepared using a polydimethylsiloxane (PDMS) block containing cylindrical protrusions on its lower surface. The PDMS block was inverted and placed flat on a surface. A 4-mm-thick rectangular pressure block containing a central through-hole measuring 11 mm in length and 7 mm in width was positioned above the PDMS block. The PDMS block was aligned to seal the through-hole of the rectangular pressure block. Next, 400 μL of hot 2.5% agarose prepared in FABG was poured into the through-hole and allowed to cool and solidify for 10 min.

After removal from the mold, the solidified agarose block was inverted to expose the circular microcavities on its lower surface. A 1.5 μL aliquot of bacterial suspension diluted 3000-fold was deposited onto the cavities. After air-drying, the agarose pad was inverted, gently pressed onto a glass-bottom culture dish, and sealed.

Fluorescence imaging of gel-based assays

Gel–glass interface, co-culture, and gel microcavity samples were imaged using an Olympus IX83 inverted fluorescence microscope. Gflamp1 and CyOFP1 fluorescence images were acquired simultaneously using 488-nm excitation and a dual-camera system equipped with two Photometrics BSI cameras. Emission was collected using FF01-515/30–25 and FF01-598/25–25 filters (Semrock) for Gflamp1 and CyOFP1, respectively. Gel microcavity experiments were imaged using a 100$\times$ objective, whereas the other gel-based experiments were imaged using a 40$\times$ objective. Fluorescence images were acquired at 5-min intervals. Image processing was performed using custom MATLAB code as previously described.[52]

Particle image velocimetry analysis

Particle image velocimetry (PIV) analysis was performed using PIVlab version 3.09.[53] Time-series CyOFP1 images were used as input. Before analysis, a constant background intensity was subtracted from all frames. Translational drift was then corrected using a discrete Fourier transform registration approach implemented with the MATLAB functions `dftregistration` and `imtranslate`.

Velocity fields were calculated using a four-pass fast Fourier transform window-deformation scheme with interrogation window sizes of 120 $\times$ 120, 100 $\times$ 100, 80 $\times$ 80, and 60 $\times$ 60 pixels. Spurious vectors were removed by manually defining validation thresholds. For each image pair, the mean u and v components of the resulting vector field were subtracted from the corresponding individual vector components. The mean flow magnitude was calculated as the arithmetic mean of all individual velocity magnitudes within the analyzed region.

Direct mechanical compression in the microfluidic device

Before use, microfluidic chips were immersed in deionized water at 4°C for at least 2 days. Before each experiment, the gas and liquid lines were connected. Phosphate-buffered saline (PBS) was injected into the gas line to displace all air, after which the outlet tubing was blocked. A 10-fold dilution of a bacterial culture at an OD_{600} of approximately 0.5 was injected into the liquid line. Bacterial adhesion was monitored by microscopy while FABG was simultaneously introduced at a flow rate of 200 μL/h.

After a sufficient number of cells had adhered, the gas line was connected to an air-pressure controller (FluidicLab PC-1). Pressure was gradually increased until the PDMS square compression pillars just contacted the glass surface; this position was defined as zero working pressure. Cells were then cultured at 30°C for 1 h. Subsequently, predefined pressure waveforms were applied to mechanically compress the cells while fluorescence images were acquired simultaneously.

Fluorescence imaging and single-cell analysis in the microfluidic compression assay

Fluorescence images were acquired using a Leica MM165 spinning-disk confocal microscope equipped with a 100× objective and two Photometrics BSI cameras for simultaneous acquisition of Gflamp1 and CyOFP1 fluorescence. B525/50 and B617/73 emission filters (Semrock) were used for Gflamp1 and CyOFP1, respectively. Images were acquired at 2-min intervals.

Image analysis consisted of three steps. First, images acquired by the two cameras were spatially registered and corrected for channel-dependent color differences. Second, individual cells were segmented from CyOFP1 images using Omnipose[54] in an Anaconda environment. The `bact_fluor_omni` model was used, and all other parameters were left at their default values. Third, cells were tracked using a custom MATLAB algorithm that identified the same bacterium in adjacent frames based on overlap between segmented regions.

Finite-element estimation of mechanical stress in gel microcavities

The mechanical force exerted on bacteria in gel microcavities was estimated using the polymer-gel framework described by Hong et al.[55] and Wang et al.[56] The model considered a simple gel in which water was the only mobile solvent, and the unloaded dry polymer network was used as the reference state. Numerical simulations were implemented in COMSOL Multiphysics version 6.0. Additional details are provided in the Supplemental Information.

Estimation of mechanical force in the microfluidic direct-compression assay

The force exerted on individual bacteria in the microfluidic direct-compression assay was estimated from the measured cell deformation using the model of Vella et al.[30] A bacterial cell was modeled as a prolate ellipsoidal elastic shell with an initial long-axis length L_0, an initial short-axis width W_0, and an internal turgor pressure p. The mechanical force F applied at the midpoint of the upper surface along the long axis was estimated as

$$F = \frac{\pi p \delta_w}{\beta \kappa_M} \quad \text{(Equation 1)}$$

where $\beta = \delta_w/\delta_D$ is the ratio of the change in cell width, δ_w, to the change in cell height, δ_D, and $\kappa_M=(\kappa_L+\kappa_W)/2$ is the mean curvature. The longitudinal and transverse curvatures were defined as $\kappa_L = 2W_0/L_0^2$ and $\kappa_W = 2/W_0$, respectively.

This approximation requires the indentation depth to be greater than the shell thickness and the shell to be in the high-internal-pressure regime, defined by $\tau \gg 1$. The dimensionless pressure parameter was calculated as

$$\tau = \frac{pR^2}{4\sqrt{EtB}} \quad \text{(Equation 2)}$$

where $R = W_0/2$ is the local radius of curvature, E is the Young's modulus of the peptidoglycan shell, t is the shell thickness, and $B = Et^3/[12(1-\nu^2)]$ is the bending stiffness. Using $t = 3$ nm,[57] $E = 100$ MPa,[58] $R = 250$ nm, and $\nu = 0.3$,[59] the pressure corresponding to $\tau = 1$ was approximately 17 kPa. A turgor pressure of 0.5 MPa[60] yielded $\tau \approx 29$, satisfying the high-pressure condition. The indentation-depth condition was also satisfied because the estimated indentation depth at the onset of cAMP activation was approximately 35–45 nm, which was substantially greater than the assumed peptidoglycan thickness.

For a representative bacterial cell, $L_0 = 2$ μm, $p = 5$ atm (approximately 0.5 MPa), and $\beta = 1$ were used. Details of the estimation of β are provided in the Supplemental Information.

Because bacterial turgor pressure depends on the growth medium, a lower turgor-pressure range of 0.05–0.08 MPa was also considered, based on the estimated osmolality of FAB medium and measurements reported by Cayley et al.[61] Using $p = 0.05$ MPa yielded $\tau \approx 3$ and reduced the estimated force at the onset of cAMP activation from approximately 30 nN to approximately 3 nN. The activation threshold was therefore reported as a model-based estimate of approximately 3–30 nN.

Bacterial adenylate cyclase two-hybrid assay

Bacterial adenylate cyclase two-hybrid (BACTH) assays were performed using the Euromedex BACTH kit according to the method of Karimova et al.[62] Coding sequences corresponding to $ChpA^N$ (amino acids 8–557), full length ChpA, $ChpA^C$ (amino acids 558–2472),

FimV^{C} (amino acids 481–919), FimV TPR3 (amino acids 844–919), and PilG were cloned into pKT25, pKNT25, PUT18 and pUT18C to generate fusions to the T25 and T18 fragments of adenylate cyclase, respectively.

Pairs of recombinant plasmids were co-transformed into *E. coli* BTH101. Transformants were selected on LB agar containing 50 μg/mL kanamycin, 100 μg/mL ampicillin, 25 μg/mL streptomycin, 40 μg/mL X-Gal, and 0.5 mM IPTG. Plates were incubated in the dark at 30°C for 48 h.

For quantitative measurement of interaction strength, β-galactosidase activity was measured in 96-well microplates according to the manufacturer's instructions. Overnight cultures were grown in LB containing 50 μg/mL kanamycin, 100 μg/mL ampicillin, 25 μg/mL streptomycin, and 0.5 mM IPTG. Cultures were diluted in M63 minimal medium, and OD_{595} was measured. Aliquots of the diluted cultures were permeabilized with SDS and chloroform and incubated with ONPG reaction buffer. After 10–20 min at room temperature, reactions were stopped by adding 1 M Na_2CO_3, and absorbance at 405 nm was measured. Activity was normalized to cell density and expressed as OD_{405}/OD_{595}. All assays were performed in at least three replicates and included vector-only controls.

Fluorescence lifetime imaging microscopy

Fluorescence lifetime imaging microscopy (FLIM) was used to assess Förster resonance energy transfer (FRET) between sYFP2 fused to ChpA^{N} as the donor and mScarlet-I3 fused to PilG or FimL as the acceptor. Harvested bacterial cells were introduced into the microfluidic device and cultured under continuous flow at 200 μL/h for 1 h at room temperature. Before FLIM acquisition, the sample was subjected to four square-wave compression–decompression cycles, each lasting 10 min. The device was subsequently maintained at low pressure (0 mbar) for 12 min before FLIM acquisition and then maintained at high pressure (40 mbar) for 12 min before a second acquisition.

FLIM measurements were performed on a Nikon Eclipse Ti2 inverted confocal microscope equipped with a DUX-VB scan head, an LUA-S6 laser unit, and an AX control module. A 515-nm LHB-104 picosecond pulsed laser operating at a repetition rate of 80 MHz was used for excitation. The optical path contained a T525lpxr dichroic mirror, and fluorescence emission was collected through an ET545/25x band-pass filter positioned before an HPM-100–40 hybrid photomultiplier tube. Images were acquired at 512 × 512 pixels with a total acquisition time of approximately 90 s per field of view. Photon arrival times were recorded using an SPC-150N time-correlated single-photon counting system to generate fluorescence decay curves.

Fluorescence lifetime analysis was performed using SPCImage 8.9 NG software (Becker & Hickl GmbH). Data were spatially binned using a binning factor of 3, and fluorescence decay curves were fitted using a biexponential model. The instrument response function was approximated using an *xexp(-x)* function to account for temporal broadening. For quantitative analysis, only donor fluorescence at bacterial poles exhibiting maximal sYFP2 intensity, corresponding to ChpA^{N} or ChpA localization sites, was included. The mean donor lifetime measured at these poles was used as the representative parameter for FRET quantification.

Estimation of apparent donor–acceptor distance from FLIM measurements

Changes in the distance between ChpA^{N} and PilG before and after mechanical compression were estimated from the sYFP2–mScarlet-I3 FLIM data using a biexponential fitting model. One decay component was fixed at 2.9 ns, corresponding to the fluorescence lifetime of sYFP2 in the absence of FRET. Fits to multiple datasets yielded the fractional population of sYFP2 molecules participating in FRET, denoted by *f*.

The amplitude-weighted mean lifetime was expressed as:

$$\tau_m = (1 - f)\tau_D + f\tau_{DA} \quad \text{(Equation 3)}$$

where τ_D and τ_{DA} are the lifetimes of the non-FRET and FRET donor populations, respectively. Values of *f* were obtained by substituting the fitted τ_m and τ_{DA} values into Equation 3. FRET efficiency was calculated as

$$E = 1 - \frac{\tau_{DA}}{\tau_D}. \quad \text{(Equation 4)}$$

The corresponding donor–acceptor distance, *r*, was determined from

$$E = \frac{1}{1+(r/R_0)^6} \quad \text{(Equation 5)}$$

where the Förster radius R_0 for the sYFP2/mScarlet-I3 pair was set to 6.3 nm, as obtained from the FPbase FRET Calculator.

QUANTIFICATION AND STATISTICAL ANALYSIS

Statistical comparisons between two groups were performed in MATLAB using the two-sample Student's *t* test implemented by the `ttest2` function. Unless otherwise stated in the corresponding figure legends, quantitative data are presented as mean ± SD. The exact values of *n*, definitions of the sampling units, measures of center and dispersion, and significance annotations are provided in the corresponding figure legends. ***, $p < 0.001$; **, $p < 0.01$; *, $p < 0.05$; ns, not significant.

For the gel–glass traffic-jamming analyses in Figures 1F and S12A, data were obtained from multiple fields of view within a single experimental run, and individual fields of view were used as the sampling units. The gel microcavity data in Figures 3C, 3D, and 4B and as well as the transcriptional-reporter data in Figure 7A, were similarly obtained from multiple fields of view, each corresponding to an individual microcavity.

For the direct microfluidic-compression experiments, data from different fields of view were pooled within each compression cycle. Three compression cycles were analyzed, and the pooled measurements from each cycle were treated as replicate observations for statistical comparison. For Figure 4F and the BACTH measurements in Figures 5B and 5C, three independent experiments were performed.

PIV-derived mean flow magnitude was calculated as the arithmetic mean of all velocity-vector magnitudes within the analyzed region. BACTH activity was normalized to culture density and reported as OD_{405}/OD_{595}. FLIM analyses used the mean donor lifetime measured at bacterial poles exhibiting maximal sYFP2 fluorescence.